Symmetry-broken double fingers and seaweed patterns in thin-film directional solidification of a nonfaceted cubic crystal

Silvère Akamatsu,[1] Gabriel Faivre,[1] and Thomas Ihle[2]
[1]*Groupe de Physique des Solides, Université Paris VII et Université Pierre et Marie Curie, CNRS URA 17, Tour 23, 2 place Jussieu, 75251 Paris Cedex 05, France*
[2]*Institut für Festkörperforschung, Forschungszentrum Jülich, Jülich D-52425, Germany*
(Received 28 November 1994)

We present a detailed experimental and numerical investigation of the directional-solidification growth patterns in thin films of the CBr_4–8 mol % C_2Cl_6 alloy, as a function of the orientation of the (fcc) crystal with respect to the solidification setup. Most experiments are performed with single-crystal samples about 10 mm wide and 15 μm thick. The crystal sometimes contains small faceted gas inclusions, the shape of which gives us direct information about the orientation of the crystal. Numerical simulations by a fully dynamical method are carried out with parameters corresponding to the experimental system. We find experimentally that, in crystals with a {111} plane (nearly) parallel to the plane of the thin film, the growth pattern is nondendritic and unsteady over the explored velocity range ($5V_c$–$50V_c$; $V_c \approx 1.9\ \mu m\, s^{-1}$ is the cellular threshold velocity). By studying the time evolution of this pattern, we establish that it is essentially similar to the "seaweed pattern" characteristic of vanishingly small capillary and kinetic anisotropies of the solid-liquid interface, recently studied numerically [T. Ihle and H. Müller-Krumbhaar, Phys. Rev. E **49**, 2972 (1994)]. The building blocks of this pattern are local structures—pairs of symmetry-broken (SB) fingers called "SB double fingers" or "doublons," and more complex structures called "multiplets"—whose lifetime is long but finite. We show experimentally that, in agreement with numerical findings, doublons obey selection rules, but do not have a preferential growth direction. We furthermore find that "dendritic" doublons also appear in crystals with a ⟨100⟩ axis close to the pulling direction (thus having a strong two-dimensional anisotropy) above a critical velocity ($\approx 20V_c$). The existence and stability of dendritic doublons in directional solidification at high velocity are confirmed by the simulations. Another crystal orientation of interest is that in which two ⟨100⟩ axes are symmetrically tilted at ±45° with respect to the pulling axis. We show experimentally and numerically that the nondendritic unsteady "degenerate" pattern observed in this case, and previously noticed by F. Heslot and A. Libchaber [Phys. Scr. **T9**, 126 (1985)], is qualitatively different from the seaweed pattern. In crystals close to this orientation, we find experimentally transitions between the degenerate and the two possible tilted dendritic states. The small amplitude of the sidebranches of dendrites in our system and the fact that the simulations with a purely capillary anisotropy do not reproduce these transitions lead us to attribute them to the increasing effect of kinetic anisotropy as the pulling velocity increases.

PACS number(s): 68.70.+w, 61.50.Cj, 64.70.Dv, 81.30.Fb

I. INTRODUCTION

Nonfaceted crystals growing from the melt can assume a variety of morphologies depending on the conditions of solidification and the physical properties of the material. Among the latter, the anisotropic properties of the solid-liquid interface—capillary energy and/or the kinetic attachment coefficient—play a particular part. It is now established that this is the anisotropy of these properties that ensures the stability of the dendrites and determines their selection rules, i.e., the relationships existing between their growth velocity, tip undercooling, and tip radius (for reviews, see, for instance, Refs. [1–4]). This naturally raises the question of the nature of the (necessarily nondendritic) growth pattern in systems with a vanishing anisotropy (as identified in viscous fingering experiments by Ben-Jacob *et al.* [5]) and of the transition between nondendritic and dendritic patterns in systems with a small but finite anisotropy (as observed in free growth of a discotic liquid crystal by Oswald, Malthête, and Pelcé [6]).

Some theoretical progress has been recently made concerning these questions by means, principally, of numerical simulations investigating the two-dimensional (2D) free growth in a channel of a crystal having a fourfold symmetry axis parallel to the axis of the channel [7–10]. In this configuration, the control parameters are the strength of the capillary anisotropy ε [defined in Eq. (4) below], the reduced undercooling Δ, and the width of the channel L, while the growth velocity V is selected by the system itself. The first important finding is that, in free growth in a channel, two branches of stationary states exist, namely, the well-known branch of symmetric (axial) fingers and the newly found branch of symmetry-broken

(SB) fingers, i.e., fingers that are not symmetric about the axis of the channel. Generally speaking, SB fingers are favored by a low anisotropy, a high undercooling, and a large spacing. More precisely, at fixed ε, SB fingers only exist above a critical value Δ_c of the undercooling, which increases as ε increases [7,10]. A metastability of the two states (axial and SB) is found within some range of undercooling above Δ_c.

Transients and unsteady permanent patterns could also be studied with the help of the dynamic numerical code used in Ref. [7], which solves the fully time-dependent equations of the problem. The simulations at $\varepsilon=0$ and with a large channel width reveal, in the first place, the existence of very long transients, with a specific, seaweed-like aspect. Depending on L and Δ, the structure finally stabilizes in a SB finger or remains permanently unsteady. In all cases, the building block of the pattern is a (possibly only transient) "SB double finger." It is a local structure consisting of two SB fingers mirror image of each other, separated by a narrow groove of liquid of constant width, called "inner" groove thereafter (Fig. 1). Like dendrites, SB double fingers obey selection rules (the tip radius of the twinned SB fingers, the width of the inner groove, and V are well-defined functions of Δ). However, contrary to dendrites, the direction of growth of the SB double fingers is not selected. In simulations at $\varepsilon=0$ and large L, SB double fingers are observed to tilt and travel along the front, without losing their individuality. This property seems to persist at small but finite ε. In Ref. [7] it was proposed to call SB double fingers "doublons" in order to emphasize their curious "solitonlike" behavior. For the sake of brevity, we shall adopt this term in the following.

In this article, we present a study of the dependence of the growth pattern on the orientation of the crystal in thin-film directional solidification of a nonfaceted cubic crystal, CBr_4 doped with 8 mol % C_2Cl_6. We shall particularly focus on the nondendritic unsteady growth pattern, which we find to exist in crystals oriented with one of their $\{111\}$ lattice planes parallel to the plane of the thin film, with the aim of establishing that this pattern is essentially the same as the seaweed pattern recently discovered in numerical simulations. Our results in directional solidification can be compared with the simulations in free growth simply by exchanging the roles played by the undercooling and the growth velocity. The condition of validity of this correspondence (V much larger than the cellular threshold velocity V_c; see Sec. IV below) is fulfilled in our experiments. We furthermore carried out numerical simulations using the same computer code as in Ref. [7] adapted to directional solidification and with parameters corresponding to the experiments.

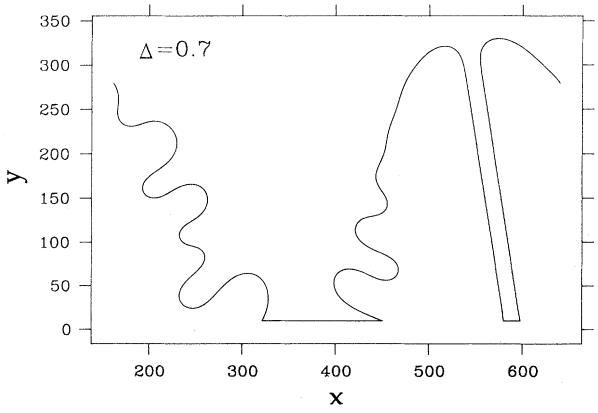

FIG. 1. A steady doublon obtained by numerical simulations in free growth with periodic boundary conditions along the x axis [7]. Capillary anisotropy, $\varepsilon=0$; reduced undercooling, $\Delta=0.7$; capillary length, $d_0=0.434$. Lengths are given in units of the grid spacing Δx (see Sec. IV).

In thin-film directional solidification, the geometry of the experiment is such that changing the orientation of the crystal with respect to the solidification setup is equivalent to changing the strength and form of the anisotropy of a 2D system. Prior to the presentation of the results, it is necessary to make some preliminary remarks concerning this relationship between crystal orientation and anisotropy. A difficulty that has sometimes been overlooked in the past is that three independent parameters are necessary to describe the orientation of the crystal with respect to the solidification setup. To take this fully, and clearly, into account, we shall always regard the crystal as "misoriented" with respect to some orientation of high symmetry, in which a lattice plane (hkl) is parallel to the plane of the thin film and a lattice axis $[uvw]$ is parallel to the pulling direction (note that $hu+kv+lw=0$). We shall denote this high-symmetry orientation $(hkl)[uvw]$ (or $\{hkl\}\langle uvw\rangle$ when we refer to the set of all equivalent orientations). The crystal itself will be said to be close to the $(hkl)[uvw]$ orientation or nearly $(hkl)[uvw]$-oriented. If necessary, its misorientation with respect to $(hkl)[uvw]$ will be described as a rotation specified by an axis and an angle of rotation. Similarly, we shall call a nearly (hkl)-oriented crystal a crystal presenting a (hkl) plane parallel to the plane of the sample, the orientation of the pulling axis being unspecified.

It will be seen below that the kinetic anisotropy plays a part in our system. We should thus take it into account. The difficulty is that we do not yet know quantitatively the respective strengths of the capillary and kinetic components. As usually done in the previous theoretical work and because only the symmetries of the anisotropy are relevant for most questions addressed in this article, we shall model our system by one in which the anisotropy is of purely capillary origin. Then, the relevant anisotropy is that of the surface stiffness in the plane of the sample

$$\tau(\alpha)=\gamma(\mathbf{n})+\frac{\partial^2\gamma(\mathbf{n})}{\partial\alpha^2}\ , \tag{1}$$

where γ is the orientation-dependent surface tension of the solid-liquid interface, $\mathbf{n}$ is the unit vector normal to

the interface (**n** is lying in the plane of the sample), and α is the angle between **n** and the pulling axis. What we need to describe is how the function $\tau(\alpha)$ [called the $\tau(\alpha)$ plot thereafter] depends on the orientation of the crystal with respect to the solidification setup. The two major experimental facts that the model must reproduce are that, over the whole explored velocity range (about 10–100 μm s^{-1}), (i) in {001}-oriented crystals, dendrites grow along the ⟨100⟩ directions of the crystal, and (ii) in {111}-oriented crystals, the growth front assumes the seaweed pattern characteristic of a low anisotropy level. The function of **n** of lowest degree consistent with the symmetry of the crystal and accounting for both facts is

$$f_4(\mathbf{n})=n_1^4+n_2^4+n_3^4 , \tag{2}$$

which is equivalent to the fourth-order cubic spherical harmonic (see the Appendix). We shall therefore assume that the orientation dependence of γ is the same as that of f_4:

$$\gamma(\mathbf{n})-\gamma_0 \propto f_4(\mathbf{n}) , \tag{3}$$

where γ_0 is the average value of γ. This leads, for the {001}⟨100⟩ orientation, to

$$\tau(\alpha)\approx\tau_0[1-\varepsilon\cos(4\alpha)] , \tag{4}$$

which is the formula assumed in most previous theoretical work, and, for the {111} orientation, to $\tau(\alpha)=$const (independent of α). Equation (3) is of course only meant to be an approximate description of the anisotropy of our system. In particular some "remnant" sixfold anisotropy is probably present in the {111} planes. However, it will be seen that this approximation satisfactorily accounts for all the observations presented in this article.

Let us end this introduction with a rapid survey of the original results provided by this study. Some indications about the experimental methods are given in Sec. II. The experimental observations are presented in Sec. III and the numerical results in Sec. IV.

In Sec. III A, in order to characterize our experimental system, we present a brief study of the dendritic regimes in crystals close to the standard (001)[100] orientation, at intermediate velocities ($V<20V_c$). We find that the effect of kinetic anisotropy on the shape of the dendrites is noticeable in the CBr_4-C_2Cl_6 system, as previously suggested by Classen *et al.* [11].

In Sec. III B, we turn to the case of nearly {111}-oriented crystals. For such orientations, for V ranging from about $5V_c$ to $50V_c$, the growth pattern is the seaweed morphology illustrated in Fig. 2. We study the time evolution of this pattern and establish that it is a set of quasistationary "seaweed cells," each cell being occupied by transient doublons, and multiplets, in conformity with the predictions of numerical simulations at vanishing anisotropy. Steady symmetry-broken structures were previously observed in various systems ("anomalous pairs" in directional viscous fingering [12], "doublets" in directional solidification of a succinonitrile-based alloy [13]), but their shape and domain of existence are markedly different from those of the doublons studied here.

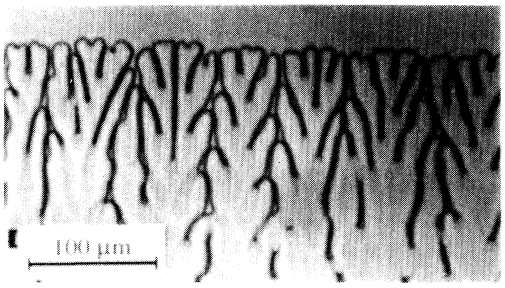

FIG. 2. Seaweed pattern in a nearly {111}-oriented crystal. The growth direction is upward, as for all the photographs in this article. The pulling velocity $V=64$ μm s^{-1} ($\approx 33.7V_{CS}$).

In Sec. III C, we return to the case of crystals close to a {001}⟨100⟩ orientation and show that, in this orientation, there exists a velocity threshold (about $20V_c$) above which "SB double dendrites" or "dendritic doublons" coexist with dendrites, again in conformity with theoretical predictions. We study the dynamics of the corresponding unsteady regime (Fig. 3). We are not aware of a previous observation of dendritic doublons in directional solidification, but dendrites with a split tip have been observed in free growth in several different systems [14].

In Sec. III D, we consider the "degenerate" orientation {001}⟨110⟩, in which two ⟨100⟩ directions are symmetrically tilted at ±45° with respect to the pulling axis. In succinonitrile crystals with this orientation, Heslot and Libchaber have previously noticed the existence of a "chaotic" pattern [15]. We confirm the existence of an unsteady pattern, at low velocities ($V<7V_c$) (Fig. 4).

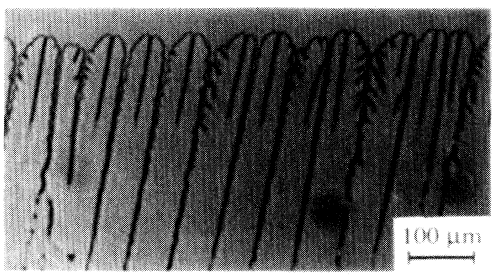

FIG. 3. Doublons in a nearly {001}⟨100⟩-oriented crystal. $V=103$ μm s$^{-1}\approx 27V_{CS}$ ($C_\infty\approx 4\%$ in this experiment).

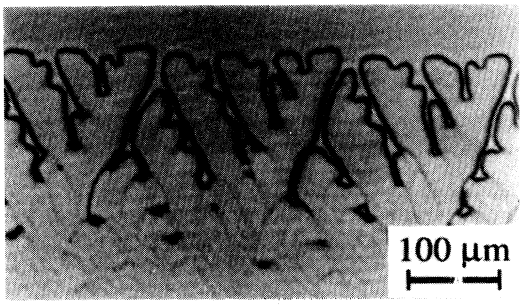

FIG. 4. Degenerate pattern in a nearly {001}⟨110⟩-oriented grain. $V=7\ \mu m\ s^{-1}$ ($\approx 3.7 V_{CS}$).

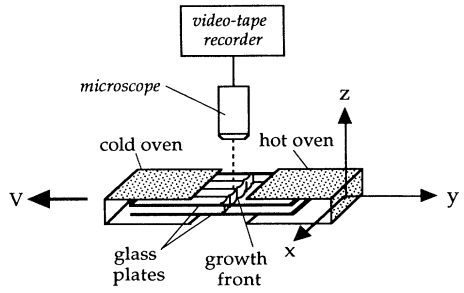

FIG. 5. Sketch of the thin-film directional-solidification setup: x, lateral direction; y, growth direction; z, transverse direction.

With the help of the numerical simulations presented in Sec. IV, we establish that the specific local feature of this degenerate regime is a finger tilted at about ±23°. The degenerate pattern is thus qualitatively different from the seaweed one.

As a conclusion of the experimental section, we present empirical stability diagrams of the CBr_4-8% C_2Cl_6 system, displaying the observed growth pattern as a function of the reduced pulling velocity and the orientation of the crystal (Sec. III E).

Section IV is devoted to the results of numerical simulations in 2D directional solidification. The three abovementioned typical orientations ({001}⟨100⟩, {111}, and degenerate) are considered in turn. The qualitative agreement between experimental observations and simulations is very good. Some experimentally observed secondary transitions (not mentioned above) are not reproduced by the simulations. This discrepancy gives us some insight into the effects of the kinetic anisotropy on the competition between different growth patterns.

II. EXPERIMENTAL METHODS

Let us briefly describe the experiments (Fig. 5). The sample is made of two parallel glass plates enclosing a thin film of a transparent alloy. This sample is placed between two ovens imposing an external, fixed thermal gradient G. The temperatures of the ovens are chosen in such a way that the solid-liquid front is located in the gap between the ovens and can thus be continuously observed with an optical microscope. A motor pulls the sample towards the cold oven at a constant velocity V. In a permanent regime, this pulling velocity is necessarily the average growth velocity of the front. Prior to pulling, the sample is held at rest in order to homogenize the concentration in the liquid ahead of the interface. The onset of pulling is followed by an instrumental transient, consisting of a slight readjustment of the temperature distribution in the sample. The time constant of this transient is about 12 s, independent of V. This transient is superimposed on the diffusive initial transient, whose time scale, given by the diffusion time $\tau_d = l_d/V$, where $l_d = D/V$ is the diffusion length (D is the diffusion constant in the liquid) is generally much shorter than 10 s at the pulling velocities considered in this article.

The dimensions of the samples are as follows. The thickness of the thin film is nominally that of the two poly(ethylene terephthalate) (PET) stripes serving as spacers between the two glass plates (12 μm). The useful length in the pulling direction is about 20 mm, the total length being 70 mm. The lateral width, limited by the PET stripes, is about 10 mm. The field of view on the video screen at the magnification used is about $600 \times 500\ \mu m^2$. This limits the size of the region of the front that can be followed continuously in time. To visualize the whole front, we must displace the X-Y stage under the microscope. In the experiments, the diffusion length is at most 200 μm, thus much smaller than the length of the sample. In some samples, the glass plates are bent in such a way that, near the middle of the sample, the thickness of the thin film is much smaller than 12 μm. We made use of such samples to check that 3D effects—which are obviously present—are unimportant as far as the qualitative conclusions of this study are concerned.

The CBr_4-C_2Cl_6 alloy is known to solidify in a fully nonfaceted way [16]. The observations reported below have been performed at one concentration $C_\infty \approx 0.08$. This value, which is just below the limit of the eutectic plateau of the alloy, is so chosen as to minimize the critical velocity V_c. At this concentration, the structure of the crystal is face-centered cubic. We shall not repeat here the details about the purity of the products, which can be found elsewhere together with other experimental details [17]. The physical properties of the CBr_4-C_2Cl_6 alloy relevant for the solidification are reproduced in Table I. They include the melting point T_m of pure CBr_4, the slope m of the liquidus, the partition coefficient K, the capillary coefficient a_0 appearing in the Gibbs-Thomson equation, and D. In Table II, we give the values of the main characteristic quantities intervening in experiments. These are the temperature of the liquidus

TABLE I. Physical constants of the CBr_4-C_2Cl_6 alloy [17] (for a definition of the symbols, see the text).

T_m (°C)	$\lvert m \rvert$ (K/mol %)	K	a_0 (μm K)	D (cm^2 s^{-1})
92.5	0.8	0.75	9×10^{-2}	5×10^{-6}

$T_{liq}=T_m-mC_\infty$, the thermal gap $\Delta T_0=m(K^{-1}-1)C_\infty$, the thermal length $l_{th}=\Delta T_0/G$, the capillary length $d_0=a_0/\Delta T_0$, and $V_{CS}=D/l_{th}$ (CS stands for constitutional supercooling), which we can assume to be a good estimate of V_c. The relative uncertainties on these values are in the range 10–20 %.

Near their melting point, crystals of CBr_4-C_2Cl_6 are fcc plastic solid solutions. They undergo a plastic-to-nonplastic transition at about 43°C. The occurrence of this transition prevents one from using such methods as an *a posteriori* determination of crystal orientations by x-ray diffraction, or seeding of the liquid with preoriented crystals. Consequently, the following methods are used to control the microstructure of the solid in our samples.

At the time when the samples are ready to be placed in the directional solidification setup, they are fully crystallized. When introduced into the setup, they partly melt, the solid-liquid front settling at the position where the temperature is T_{liq}. At the end of this process, the front is polycrystalline and generally contains about ten grains, apparently random in orientation. Grain boundaries are revealed by the cusps they form at the interface. Each time the sample is remelted, a new set of about ten randomly oriented grains is obtained. In this way, any desired orientation can be obtained, at least approximately.

With such polycrystalline samples, it is possible to observe the morphologies corresponding to different orientations under strictly identical growth conditions. The reduced undercooling $\Delta=(T-T_{liq})/\Delta T_0$ of the most advanced point of the pattern is an important variable. It is exactly 1 at the planar front (which settles at $T=T_m-mC_\infty/K$) and less than 1, but still of order 1, at the cell or dendrite tips. Absolute measurements of Δ are possible, but difficult to perform and not very precise. On the other hand, it is easy to measure the difference of undercooling $\delta\Delta$ between the patterns in neighboring grains with a good accuracy (about 10^{-2}).

On the other hand, experiments with single crystals are achieved as follows. A channel narrower than the typical width of the initial grains is formed by cutting the PET spacers in such a way as to delimit a funnel-shaped free space (Fig. 6). After the crystal has spread out laterally

TABLE II. Values of some quantities characterizing the experiments (for a definition of the symbols, see the text).

C_∞ (mol %)	G (K cm^{-1})	ΔT_0 (K)	l_{th} (μm)	d_0 (μm)	V_{CS} (μm s^{-1})
8	80	2.2	270	0.054	1.9

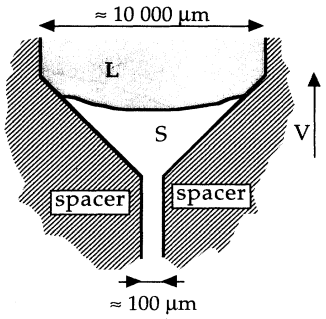

FIG. 6. Sketch of the method of obtaining single crystals (L, liquid; S, solid).

over the whole width of the sample, the pulling is stopped in order to homogenize the liquid and check that no grain boundary emerges at the solid-liquid interface. These experiments have shown that the size of the grain is by no means an important factor, as far as the characterization of permanent structures is concerned, provided the grain size is larger than about five spacings of the pattern. In other words, the width of the perturbed region about the grain boundaries does not exceed two spacings. It is worth noting that this observation (like many others) indicates that phase diffusion is extremely slow in all deep-cell regimes.

Experiments with single crystals have evidenced that subgrain boundaries are created in the crystals during the growth (polygonization during growth). It is observed that a growth front initially free of grain-boundary cusps always bears some very shallow ones after a high-velocity pulling. These correspond to subgrain boundaries with very small misorientations. We do not know with certainty the mechanism by which these defects are created. It is probably similar to the one recently discovered experimentally by Grange *et al.* in the directional solidification of Al-Cu crystals [18]. In brief, these authors show that bundles of dislocations are attached to the bottom of the liquid grooves between the cells. From time to time, for some unknown reason, one of the bundles emits a subgrain boundary across one of the neighboring cells, which then becomes misoriented with respect to the others. The corresponding misorientations are less than 0.1°. Such small misorientations are not likely to have a large influence on the growth patterns. However, we shall show below (Sec. III C) that, after a long time of pulling, an accumulation of very-small-angle subgrain boundaries has occurred, leading to misorientations large enough to significantly perturb the solidification dynamics.

In thin-film directional solidification, it is common practice to deduce the orientation of the crystal from the characteristics of the growth pattern, for instance, the tilt angle of the dendrites. In the present study, first, we extend this method by correlating more systematically the three orientation variables with the nature of the pattern. Second, we cross-checked the results of this correlation by making use of the occasional existence of small

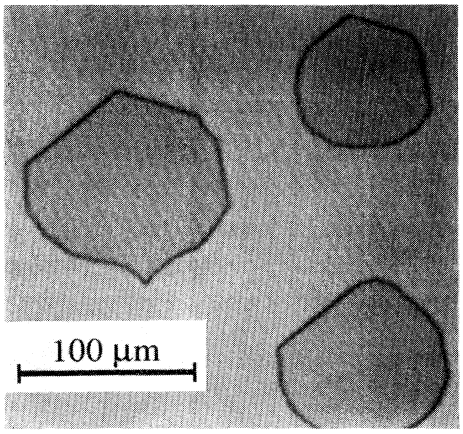

FIG. 7. Partly faceted residual-gas inclusions in a nearly {111}-oriented crystal. Note that the orientation of the facets is the same in all the inclusions.

residual-gas inclusions in our crystals [17]. It was shown by Pavlovska and Nemow [19] that a gas bubble included in an isothermal crystal of CBr_4 becomes faceted below about 80°. Since facets have a definite crystallographic nature, one can deduce the orientation of the crystal in the laboratory frame from the image of a faceted bubble enclosed in it. Our samples are not isothermal, but submitted to a thermal gradient. Consequently, the gas inclusions are not at rest, but migrate towards high temperatures [20] (their migration velocity is about 0.2 μm s^{-1}). Nevertheless, the part of the interface that is concave with respect to the direction of migration is faceted. By studying the shape of such bubbles in various grains, we reached the conclusion that the largest facets lie on the {100} lattice planes. We are thus in a position to determine *in situ* the orientation of the growing crystal if it happens that a gas bubble is trapped in it. The accuracy of the method is about ±2°. Figure 7 shows bubbles included in a crystal, which, on solidification, exhibited a seaweed pattern. The 120° angles between the facets of the bubbles confirm that a {111} axis is normal to the plane of the sample (a more precise analysis shows that the deviation from the {111} orientation is less than 3°). The same type of direct confirmation of the orientation of the crystal could be obtained for {001}⟨100⟩- and {001}⟨110⟩-oriented crystals.

III. EXPERIMENTAL RESULTS

A. Dendrites in crystals close to the standard (001)[100] orientation

In the velocity range 10–40 μm s^{-1}, for most orientations of the crystal, the growth pattern is dendritic and stationary (apart from slow rearrangements of the spacings, which we need not to consider here). Most generally, the dendrites are tilted, i.e., they drift along the front at a constant velocity V_d. We measured the (in-plane) tip radius R of the dendrites, by fitting a parabola onto their profile, and their tilt angle $\phi=\tan^{-1}(V_d/V)$, as functions of V in a series of grains. In some of them, the orientation could be deduced from the shape of a gas inclusion in the solid. The main conclusions of this study are as follows.

In all grains, in conformity with the well-known properties of dendrites in directional solidification, R is a decreasing function of V. In the grains in which dendrites are tilted, ϕ increases as V increases, approaching a constant value ϕ_∞, which is practically reached at about $10V_{CS}$ [21,22]. In all cases in which the orientation of the grain is known, we verified that, within experimental uncertainty, $\phi_\infty=\alpha_0$, where α_0 is the angle of the pulling direction with the projection of a ⟨100⟩ axis in the plane of the sample. Large values of ϕ_∞ (30°–55°) are frequent. Grains with values of ϕ_∞ larger than about 30° will be left aside for the moment and considered later on in Sec. III D.

Concerning the profile of the dendrites, we find that the majority of the grains can be divided into two groups according to the following criteria. The first group contains grains in which, at fixed V, R has the same value R_M, independently of ϕ. In the second group, R is larger than R_M and is grain dependent. From the selection rules established numerically in directional solidification for capillary [23] as well as for kinetic [11] dendrites, it is clear that the anisotropy is at its highest possible level in the first group, while it is weaker, and orientation dependent in the second group. This can be easily rationalized if it is admitted that the orientation dependence of the strength of the anisotropy, either capillary or kinetic, is well described by the fourth-order cubic spherical harmonic. Let us assume, as above, that the anisotropy is of purely capillary origin. For orientations sufficiently close to (001)[100], $\tau(\alpha)$ can be approximately described by (see the Appendix)

$$\tau(\alpha)\approx\tau_0[1-\varepsilon\cos4(\alpha-\alpha_0)]\ , \tag{5}$$

where ε is the (orientation-dependent) effective anisotropy level and α_0 the angle of the first minimum of τ to the pulling direction. In the perfect (001)[100] orientation, $\alpha_0=0$ and ε takes its highest possible value ε_M. A rotation of the crystal about the [001] axis ("in-plane" misorientation) changes α_0, but not ε (which remains equal to ε_M). The misorientation must include a rotation about [010] ("off-plane" misorientation) for ε to be smaller than ε_M. It is then clear that, since R is a decreasing function of ε at fixed V, the off-plane misorientation is small in the grains of the first group and large in the grains of the second group. From the known orientation of some grains, we can deduce that, for its effect to be measurable, the off-plane misorientation must be larger than 20°.

Figure 8 shows the profile of dendrites in a grain with a small off-plane misorientation at two different velocities (13 μm s$^{-1}\approx6.8V_{CS}$ and 35 μm s$^{-1}\approx18V_{CS}$). The corresponding values of various quantities of interest are

TABLE III. Values of some characteristic properties of the dendrites shown in Fig. 8 (for a definition of the symbols, see the text).

Case	V (μm s^{-1})	λ (μm)	R (μm)	ϕ (deg)
Figure 8(a)	13	100	7.0±0.5	5±1
Figure 8(b)	35	125	4.5±0.5	7±1

given in Table III. They indicate that the in-plane misorientation of the grain is about 7°. For comparison with the literature, it is worth mentioning that $R^2V \approx 700 \pm 100$ μm^3 s^{-1} and $d_0 l_d / R^2 \approx 0.06 \pm 0.01$. These values are not very different from those previously found by other authors in CBr_4-based alloys [24,25]. However, we observed that the dendrite profiles rapidly deviate from the parabola, this deviation being more pronounced as the velocity is increased. This is illustrated in Fig. 8(b), which shows that, at 35 μm s^{-1}, the shape of the dendrite tip is quasitriangular. Furthermore, at 13 and 35 μm s^{-1}, although the spacing is large ($> 3l_d$), sidebranches are hardly visible. According to numerical simulations by Classen *et al.* [11], these features are most probably attributable to kinetic effects (Mergy *et al.* [17] formerly stated that no kinetic effect is detectable on the recoil of the planar front at low pulling velocities; this does not contradict our present conclusion, since Classen *et al.* point out that a strong effect of the kinetic anisotropy on the shape of the dendrite is compatible with a very small average value of the kinetic coefficient).

Figure 9 shows a dendrite in a grain with a strong off-plane misorientation (the analysis of the shape of a gas inclusion showed that this grain is in fact relatively close to a {111} orientation, the angle between the {111} plane and the plane of the sample being about 7°), at practically the same velocity as in Fig. 8(a). It can be seen that this dendrite bears much larger sidebranches than those in nearly (001)[100]-oriented grains, which, according to Ref. [11], probably means that the anisotropy of the kinetic coefficient decreases as the off-plane misorientation increases. This is clearly compatible with the kinetic coefficient varying with orientation as the fourth-order cubic spherical harmonic.

Finally, we measured the differences of reduced undercooling between (001)[100] and off-(001)[100] dendrites. The latter invariably have a higher undercooling than the former, the difference being at most 0.10. We did not attempt to measure the absolute value of Δ. We recall that the reduced tip undercooling of a purely capillary dendrite can be approximately calculated from the geometrical Péclet number $\mathrm{Pe} = VR/2D$ with the help of the Ivantsov relationship [see Eq. (11) below]. The value found in this way for the (001)[100] orientation is $\Delta_{I_v} \approx 0.5$ at $V \approx 35$ μm s^{-1}.

Further, careful studies would obviously be necessary to determine more quantitatively the strength of the capillary and kinetic effects. Fortunately, for accounting for the preceding results, it is sufficient to know that the anisotropy, whatever its nature, is well described by the fourth-order cubic spherical harmonic. In the calculations presented in Sec. IV, we use the value $\varepsilon = 0.12$ of the coefficient of capillary anisotropy, which is such that the tip radius of the calculated dendrites is the same as

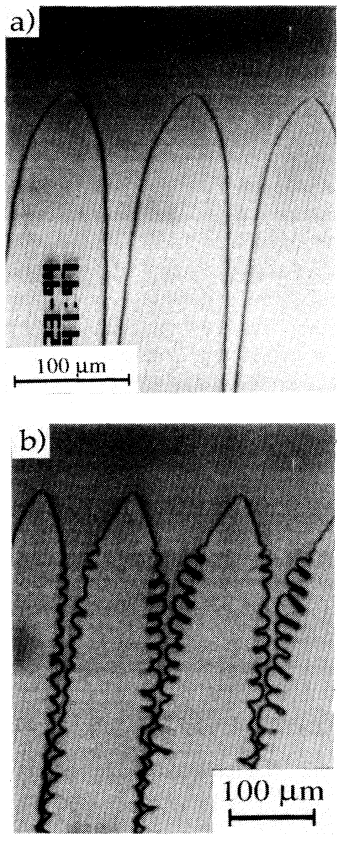

FIG. 8. Dendrite tips in a nearly {001}⟨100⟩-oriented crystal (see Table III). (a) $V = 13$ μm s^{-1}; (b) $V = 35$ μm s^{-1}.

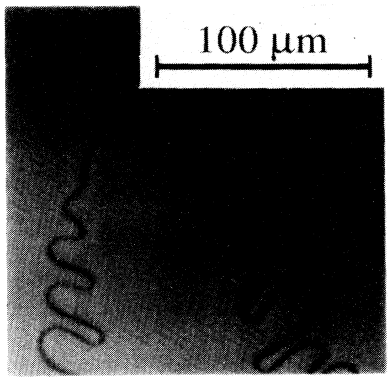

FIG. 9. Dendrite tip in a crystal relatively close to a {111} orientation (off-plane misorientation angle ≈7°). $V = 14$ μm s^{-1}.

the experimental tip radius in (001)[100]-oriented grains at $V \approx 30\ \mu m\ s^{-1}$ (see Table III).

B. Seaweed morphology in nearly {111}-oriented crystals

1. The seaweed pattern at high velocities

Figure 10 shows the pattern observed in a grain close to a {111} orientation for velocities ranging from about $5V_{CS}$ to $50V_{CS}$. The similarity between this pattern and the seaweed morphology found in the numerical simulations at zero anisotropy leaves no doubt that the anisotropy for this orientation of the crystal is very weak. There are several ways of establishing that this "seaweed pattern" is a true permanent regime of the system for the orientation considered. One of them is to show that it corresponds to a well-defined undercooling, different from (and larger than) that of the dendritic states observed for other orientations. Figure 11 shows two adjacent grains in a polycrystal, one in the seaweed state and the other in a tilted dendritic state. We measured the corresponding values of $\delta\Delta$ as a function of V. We find that $\delta\Delta$ increases from 0.12 to 0.16 (± 0.01) as V/V_{CS} increases from 5 to 50. Thus the difference of undercooling between seaweed and dendritic states is larger than between any two dendritic states, in agreement with numerical results (see Sec. IV).

Another fact attesting to the well-defined nature of the seaweed pattern is the permanency of its morphological characteristics over a finite velocity range. This is obvious from Fig. 10 for the two intermediate velocities ($V \approx 10V_{CS}$ and $33.5V_{CS}$), but less clear for the two extreme ones ($V \approx 4.5V_{CS}$ and $52V_{CS}$). We shall show in Sec. III B 2 that a qualitative transformation of the pattern really takes place below about $5V_{CS}$. On the other hand, a 3D breakdown of the 2D seaweed pattern is to be expected at high velocity, when some characteristic length becomes much smaller than the thickness of the film. It is this breakdown that is perceptible at $53V_{CS}$ [Fig. 10(d)]. As far as we can see, it has nothing to do with an intrinsic instability of the 2D seaweed pattern.

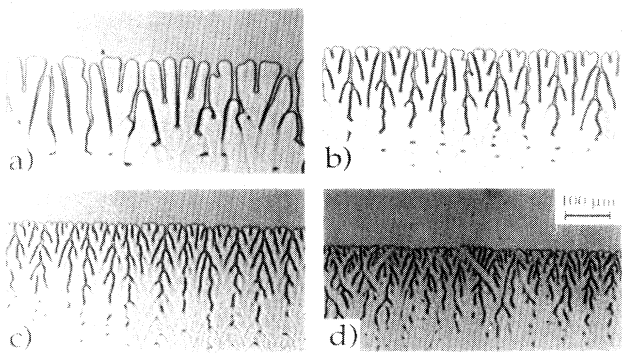

FIG. 10. Seaweed morphology in a crystal close to the {111} orientation. (a) $V = 8.6\ \mu m\ s^{-1}$ ($\approx 4.5V_{CS}$); (b) $V = 29\ \mu m\ s^{-1}$ ($\approx 15V_{CS}$); (c) $V = 64\ \mu m\ s^{-1}$ ($\approx 34V_{CS}$); (d) $V = 100\ \mu m\ s^{-1}$ ($\approx 53V_{CS}$).

The analysis of the seaweed pattern that follows relies on the distinction between two types of liquid grooves, the wide and the narrow grooves. In order to establish the relevance of this distinction, we carried out spatiotemporal (ST) diagrams of the pattern, at various velocities, in the following way. At regular time intervals, a line normal to the growth direction is drawn at a given distance behind the foremost point of the front and the positions of the intersections of this line with the solid-liquid interface are measured. Then, these positions are plotted as a function of time, giving the "trajectories" of the groove walls. A ST diagram at $V = 34V_{CS}$ is shown in Figs. 12 and 13. For clarity, only the trajectories of the points at the centers of the liquid grooves are shown. It can be seen that, for times of the order of $100\tau_d$, the trajectories of the wide grooves (bold lines) are essentially straight lines parallel to the growth axis. Thus the wide grooves—and the entities (seaweed cells) between them—are quasisteady features of the pattern. In contrast, the narrow grooves (thin lines) always disappear in a finite time by merging into a wide groove.

Let us first focus on the seaweed-cell spacing λ. Figure 13 reveals that the distribution of λ is not perfectly steady, but undergoes a slow rearrangement process. During this process, the cells whose spacings happen to fall out of the stable interval are rapidly eliminated either by pinching off or splitting. We measured histograms of λ at various velocities and times (Fig. 14). It can be seen that the stability bounds and the average value of the stable cell spacings decrease more slowly than l_d, as V increases. Consequently, the average reduced spacing $\langle\lambda\rangle/l_d$ is an increasing function of V.

Returning to the narrow grooves, Fig. 12 clearly shows that their lifetime, although finite, is generally much larger than the diffusion time. This suggests that the local structures attached to the narrow grooves are doublons. A suggestive example is given in Fig. 15. The relatively narrow ($L \approx 2$) seaweed cell shown in this figure is clearly reminiscent of the doublons found numerically in free growth in a channel for similar spacings. In order to confirm that the narrow grooves are in fact inner grooves of doublons, we measured the width W of a large number of narrow grooves at each velocity. The results are displayed in Fig. 16 together with some numerical values (see Sec. IV). The experimental values of W are smaller than the numerical ones by a factor of about 2, the deviation increasing as V increases. This discrepancy partly stems from the 3D effects. The walls of the inner grooves in the experiments are curved in such a way that we do not measure the real, average width of the grooves, but a smaller, apparent width, the deviation between the two quantities increasing as the ratio of W to the film thickness decreases.

The preceding observations leave little doubt that the long-lived local structures surrounding the narrow grooves are transient doublons. This conclusion is further supported by numerical simulations confirming the existence of seaweed cells and doublons in directional solidification (see Sec. IV). It is less sure, but nevertheless

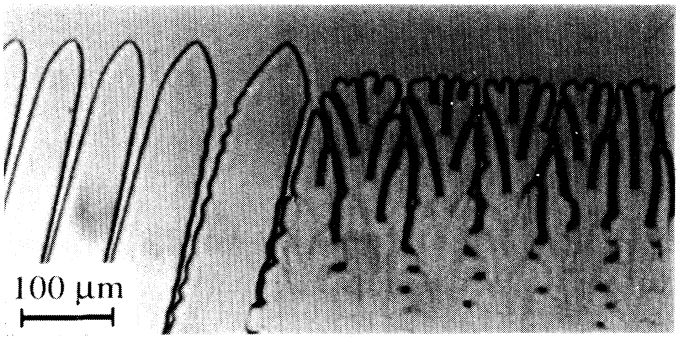

FIG. 11. Grain boundary between a tilted-dendritic grain and a seaweed grain. $V=29\ \mu m\ s^{-1}$ ($\approx 15 V_{CS}$).

likely, that "multiplets" also exist, in addition to doublons. By multiplet we designate a local structure consisting of (at least) two narrow grooves running close to each other for very long times. Stationary multiplets have been found in previous numerical simulations [7]. A multiplet (here, a triplet) can be seen, for instance, in Fig. 17. Moreover, the ST diagram in Fig. 12 indicates that multiplets are frequent when the seaweed cells are wide ($L>5$).

Let us now consider the question of the stability of doublons. In a seaweed cell, doublons are observed to appear through a tip-splitting instability at a point that is generally not the foremost one of the front. The initial growth direction of a doublon thus created is roughly parallel to the local normal to the interface. So, in general, the doublon is tilted and after some time reaches the nearby wide groove in which it disappears, being advected along it (see Fig. 17). Almost immediately, a tip-splitting instability again takes place, giving rise to a new doublon (there seems to exist conditions under which this process of elimination or creation of doublons is a quasi-periodic one; see Fig. 20). Even doublons that, within experimental accuracy, seem axial (Fig. 15) become progressively tilted after a relatively long period of apparent stability and are eliminated. From these observations, it is natural to conclude that doublons are unstable to tilting and that this instability of a peculiar nature is responsible for the unsteadiness of the seaweed pattern on the scale of a seaweed cell.

The numerical simulations performed in directional solidification at $\varepsilon=0$ (see Sec. IV) show patterns consisting of doublons. After a simulation time of the order of $20\tau_d$, the pattern is still unsteady, especially at the lowest velocity explored. In addition, our observed permanent

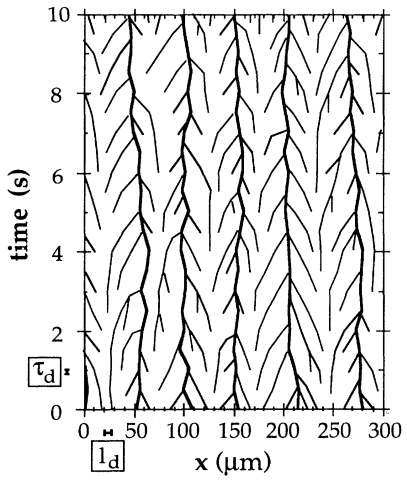

FIG. 12. Spatiotemporal diagram of the seaweed pattern shown in Figs. 2 and 10(c). $V=64\ \mu m\ s^{-1}$ ($V\approx 34 V_{CS}$; $l_d=7.8\ \mu m$; $\tau_d=0.12$ s). The trajectories plotted are those of the centers of the liquid grooves. Thick lines, wide grooves; thin lines, narrow grooves. The reference line is 10 μm behind the foremost point of the front. The time interval between measurements is 0.5 s. The record begins about 30 s after the onset of the pulling, which ensures that instrumental and diffusive transients are finished.

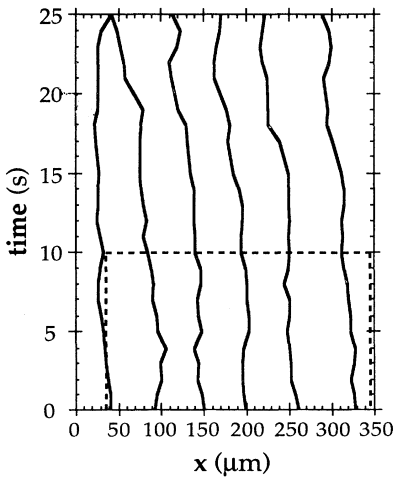

FIG. 13. Same as in Fig. 12. For clarity, the trajectories of the narrow grooves are not displayed. Dashed frame, region shown in Fig. 12.

pattern much resembles the numerical transients found in free growth in a channel at $\varepsilon=0$, large L, and large Δ. The fact that, in the latter simulations, the system eventually settles in a steady state is probably due to the constraints imposed on the system, i.e., either rigid walls with reflecting conditions (the steady state is then a SB finger running close to one of these walls) or periodic boundary conditions (the steady state is a periodic array of axial or tilted doublons) [7,26].

2. *Transformation of the pattern at low velocity*

The above characterization of the seaweed pattern poses no problem as long as the distinction between wide and narrow grooves is clear. This distinction becomes less and less so as V decreases. Figure 18 shows a seaweed grain (not the same as in Fig. 10) at velocities corresponding to $2.1V_{CS}$, $4.5V_{CS}$, and $17V_{CS}$. The corresponding ST diagrams at $2.1V_{CS}$ and $4.5V_{CS}$ are given in Figs. 19 and 20 (a slow lateral drift of the seaweed cells can be noted; it will be considered in the next subsection). At $V=4.5V_{CS}$, the pattern is of the seaweed type, as evidenced by the clear contrast between wide and narrow grooves in the ST diagram. On the contrary, at $V=2.1V_{CS}$, this distinction can no longer be made. Some branchings are indeed observed in the ST diagram,

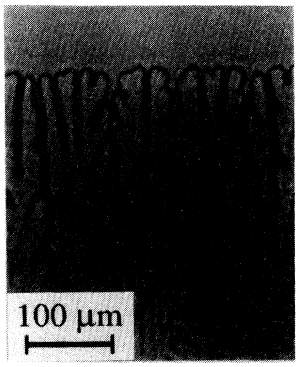

FIG. 15. A seaweed cell containing one doublon whose lifetime was about 30 s ($\approx 60\tau_d$). $V=32\ \mu m\,s^{-1}$ ($\approx 17V_{CS}$).

but it is not clear whether they correspond to transient doublons, as in the seaweed regime, or to the creation of new cells belonging to the branch of symmetric solutions.

A "transition" is thus taking place at some velocity between $2.1V_{CS}$ and $4.5V_{CS}$. This fact in itself is not surprising. Approaching the cellular threshold, one

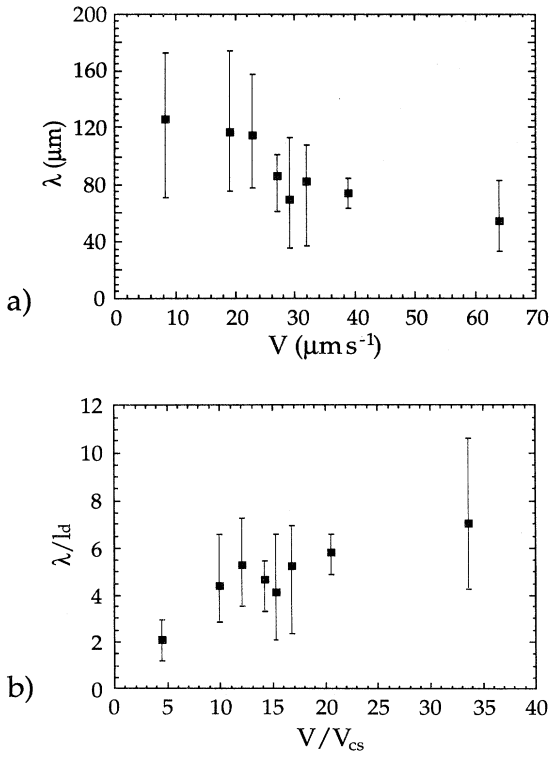

FIG. 14. Seaweed-cell spacing λ as a function of velocity: (a) absolute values; (b) reduced values. Squares, average values; extremities of the bars, upper and lower stability bounds.

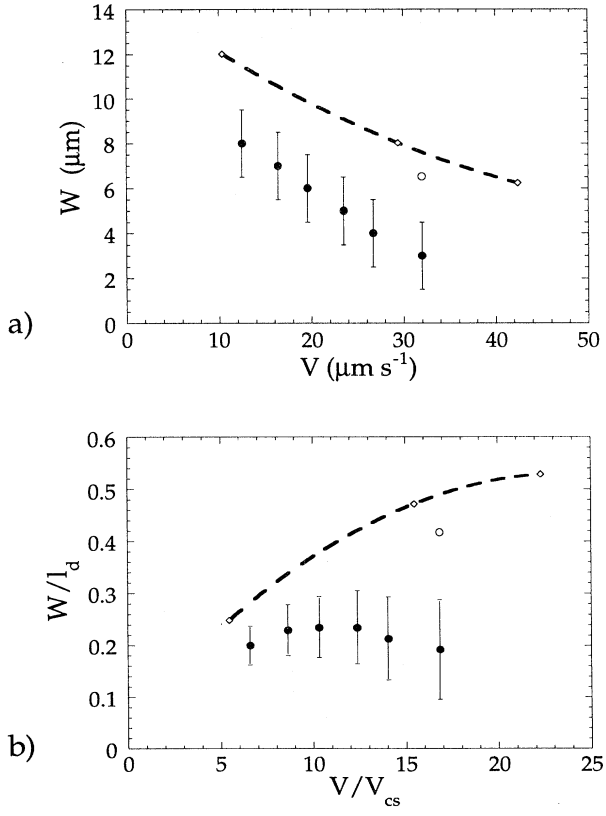

FIG. 16. Width W of the inner grooves of doublons as a function of velocity. ●, experimental measurements; ○, numerical simulations in directional solidification; ◇, numerical simulations in free growth. (a) Absolute values. (b) Reduced values.

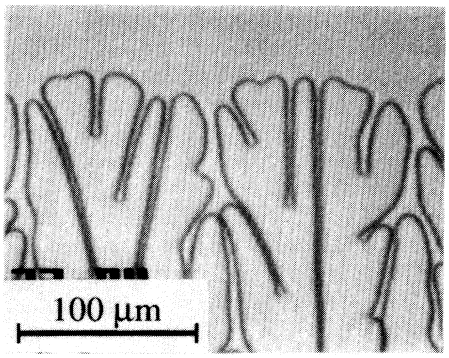

FIG. 17. Enlarged view of a seaweed pattern. $V=32\ \mu m\,s^{-1}$ ($\approx 17V_{CS}$). Note, from left to route, a doublon joining a wide groove, a newly created doublon, and a triplet structure.

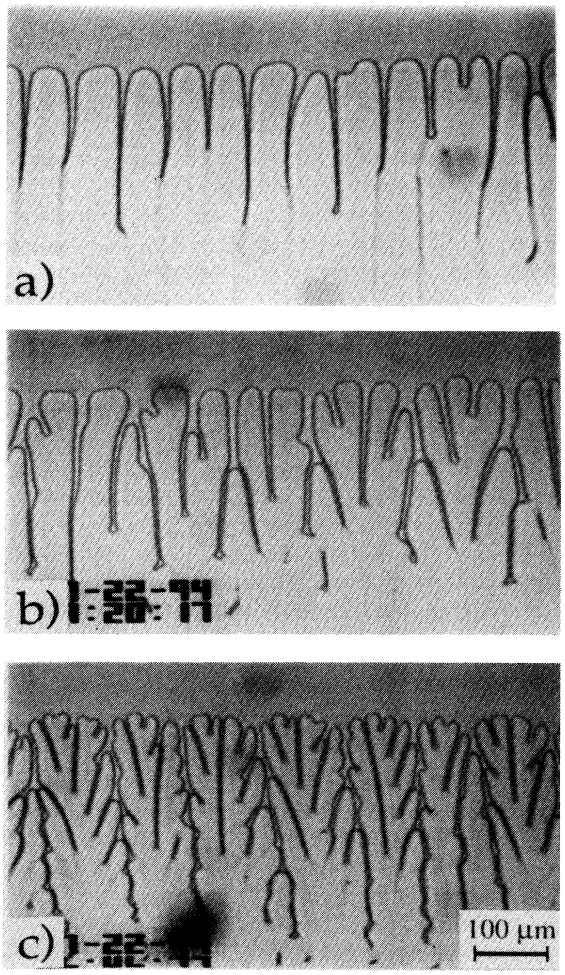

FIG. 18. The low-velocity transition in a nearly {111}-oriented grain. (a) $V=4\ \mu m\ s^{-1}$ ($\approx 2.1V_{CS}$). (b) $8.5\ \mu m\,s^{-1}$ ($\approx 4.5V_{CS}$); (c) $32\ \mu m\,s^{-1}$ ($\approx 17V_{CS}$).

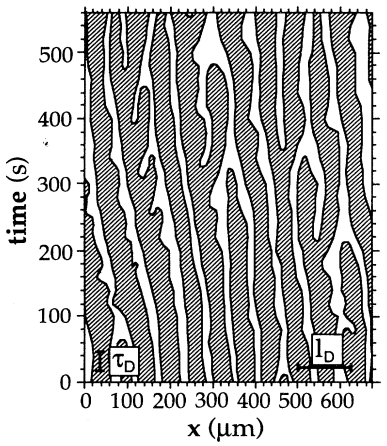

FIG. 19. Spatiotemporal diagram of the pattern shown in Fig. 18(a). $V=4\ \mu m\ s^{-1}$ ($V\approx 2.1V_{CS}$; $l_d\approx 125\ \mu m$; $\tau_d\approx 31.3$ s). The trajectories of the two sides of the grooves are represented. The time $t=0$ corresponds to 200 s ($\approx 7\tau_d$) after the onset of the pulling. Hatched regions, solid phase. The reference line was 20 μm behind the foremost point of the front. The time interval between measurements is 10 s.

enters the domain in which the stabilizing role played by the thermal gradient is certainly not negligible (this domain is that of the so-called cell-to-dendrite transition, in strongly anisotropic grains). The unexpected fact is that the regime observed at $2.1V_{CS}$ is unsteady, while a steady cellular regime is expected to exist just above V_{CS}. This point is currently under study.

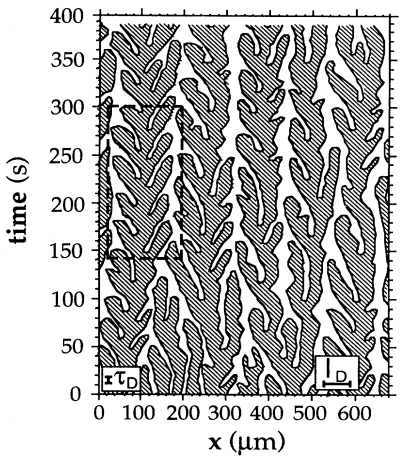

FIG. 20. Spatiotemporal diagram of the pattern shown in Fig. 18(b). $V=8.5\ \mu m\ s^{-1}$ ($V\approx 4.5V_{CS}$; $l_d=58.8\ \mu m$; $\tau_d=6.9$ s). The time $t=0$ corresponds to 155 s ($\approx 22\tau_d$) after the onset of the pulling. In the dashed frame a quasiperiodic behavior is shown.

3. *Tilted seaweed patterns*

We mentioned above that the seaweed pattern shown in Fig. 18 is slightly tilted. A clearer example of tilted seaweed pattern is given in Fig. 21. It can be seen that, at high velocities [Figs. 21(b) and 21(c)], the wide grooves limiting the seaweed cells have a tilted trajectory (tilt angle $\approx 10°$), while the directions of the transient doublons and multiplets seem unaffected by the drift of the seaweed cells. On the other hand, the low-velocity transition mentioned in the preceding subsection is more pronounced and occurs at a higher velocity ($\approx 7V_{CS}$) in the case of tilted seaweed patterns [Fig. 21(a)].

We observe that the tilt angle of the pattern is a well-defined property of the considered grain. It is most probably due to the breaking of the underlying crystallographic symmetry of the system. This means that, in crystals exhibiting a tilted seaweed pattern, (i) the anisotropy is not strictly zero and (ii) the orientation is such that no mirror plane is normal to the growth front. For clarity, let us reintroduce the orientation variable $\langle uvw \rangle$ and choose $(111)[11\bar{2}]$ as the high-symmetry orientation to which misorientations are referred. In this orientation, the $(1\bar{1}0)$ mirror plane is perpendicular to the growth front. It is very probable that, in this orientation, the seaweed pattern is nontilted and remains so for (slight) off-plane misorientations corresponding to a rotation about the $[1\bar{1}0]$ axis. On the contrary, they are tilted if the misorientation has an in-plane component breaking the symmetry about the $(1\bar{1}0)$ plane. Experimentally, some grains exhibiting a tilted seaweed pattern contained gas inclusions, allowing us to note that they had a significant off-plane misorientation ($\approx 3°$). It thus seems (but a direct proof is lacking) that the remnant sixfold anisotropy in the $\{111\}$ plane is not sufficient to induce a tilting of the pattern, when the pulling axis is not along the $[11\bar{2}]$ axis.

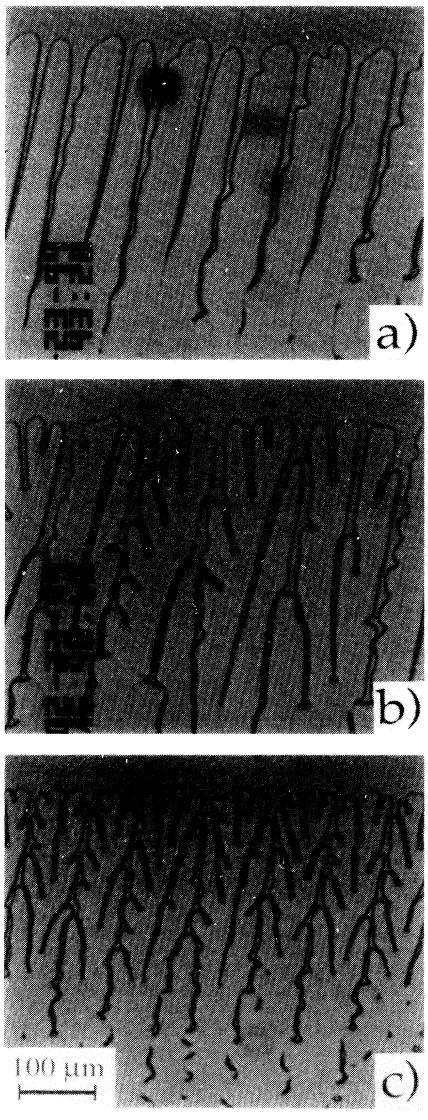

FIG. 21. Tilted-seaweed morphology in a crystal close to (but not exactly in) the (111) orientation. (a) $V=12.5$ μm s^{-1} ($\approx 6.5V_{CS}$); (b) $V=19.6$ μm s^{-1} ($\approx 10.3V_{CS}$); (c) $V=32$ μm s^{-1} ($\approx 16.8V_{CS}$).

In fact, with the help of grains containing faceted bubbles, we could establish that the maximum off-plane misorientation angle beyond which the pattern no longer belongs to the seaweed type is less than 5°. Such a small range of existence of the seaweed pattern is in agreement with the calculations reproduced in the Appendix, showing a rapid increase of ε as the misorientation with respect to $\{111\}$ increases (see Fig. 35). The type of pattern observed for off-plane misorientations larger than 5° is either dendritic (as in Fig. 9) or degenerate according to the exact nature of the misorientation (this will be explained in some detail in Sec. III E). In one grain—thus at fixed orientation—we observed an abrupt transition from a tilted seaweed pattern at V lower than about $16.8V_{CS}$ (32 μm s^{-1}) to a degenerate pattern at larger V. The grain in which this transition was observed presumably had a relatively large misorientation and thus a non-negligible kinetic anisotropy. If this is true, increasing V was qualitatively equivalent to increasing the effective anisotropy, which can explain the occurrence of the seaweed-to-dendrite transition.

C. Doublons in strongly anisotropic grains

1. *Dendritic doublons at high velocity*

We now return to grains with a strong anisotropy. In these grains, we observed that doublons composed of two symmetry-broken dendrites appear above a velocity threshold of the order of $20V_{CS}$. Figures 22 and 23 show the growth front in such a grain during two successive runs at $V=54V_{CS}$. The ST diagram corresponding to the second run is displayed in Fig. 24. A faceted bubble was included in this grain, allowing us to determine its orientation. By calculating the $\tau(\alpha)$ plot in the approximation defined by Eq. (5), we find $\varepsilon/\varepsilon_M \approx 0.6$ and $\alpha_0 \approx 2°$ to the left. At $V \approx 8.4V_{CS}$, the growth pattern is the standard dendritic one, already studied in Sec. III A. At

$V \approx 54 V_{CS}$ [Fig. 22(d)], an unsteady pattern is observed, which contains well-defined quasistable doublons. At the intermediate velocity $V \approx 18 V_{CS}$, doublons are transitorily observed, indicating that the threshold velocity for the existence of doublons is slightly below this velocity, in this grain.

The fact that, at finite ε, doublons only appear above a threshold velocity and then coexist with dendrites is in agreement with the predictions of the dynamic simulations in free growth. In the above experiment, we moreover observed that (i) at $V \approx 54 V_{CS}$, the total width of the doublons, reduced by the diffusion length, is about 20, larger than the stable reduced spacings of single dendrites by a factor about 2.5; (ii) the reduced width of the inner groove, although difficult to measure, is clearly less than 1; and (iii) the tilt angle of the doublons is not constant, contrary to that of the nearby dendrites (Fig. 24). These features are similar to those of the doublons observed in {111}-oriented crystals. There are, however, some differences and it is perhaps necessary to give a special name—"dendritic" doublons or double dendrites—to the doublons observed in dendritic grains. In particular, (i) the tips of the SB dendrites forming the dendritic doublons retain the triangular shape of the symmetric dendrites and (ii) dendritic doublons are tilted (on average) to about the same angle as dendrites (see Figs. 23 and 24), suggesting that the strong anisotropy of the crystal forces them to remain close to a ⟨100⟩ axis.

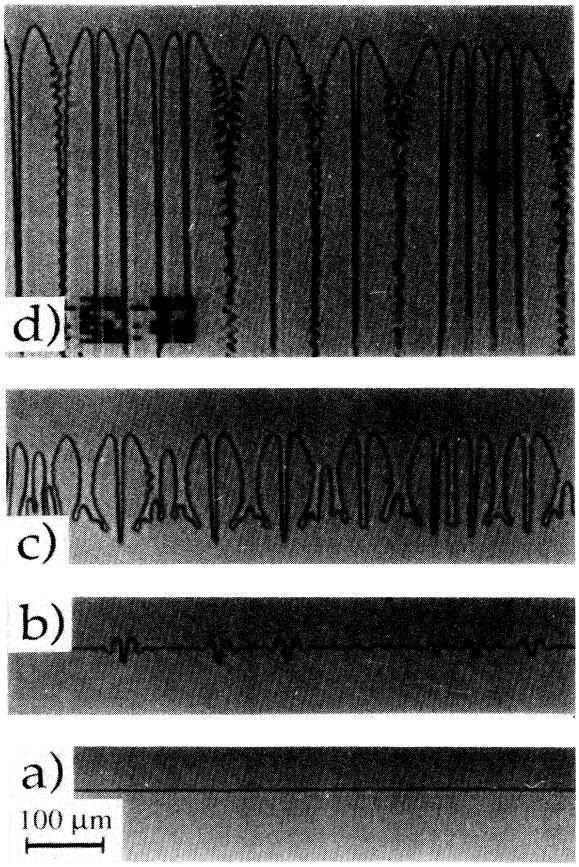

FIG. 22. Crystal close to the (001)[100] orientation. Initial transient of the first run at $V = 103\ \mu m\,s^{-1}$ ($V \approx 54 V_{CS}$; $l_d = 4.9\ \mu m$; $\tau_d = 0.05$ s). (a) $t = 0$ s (onset of the pulling); (b) $t = 6.4$ s; (c) $t = 8.1$ s; (d) $t = 42$ s. Note the dendritic doublons in the middle and the multiplet on the right. The tilt angle of the dendrites is about 2°, with a negligible dispersion.

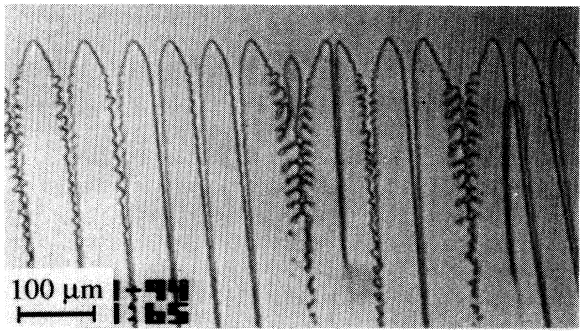

FIG. 23. Same grain as in Fig. 22. Second run at $V = 103\ \mu m\,s^{-1}$. The tilt angle of the dendrites is 5°±2°. This figure corresponds to $t = 90$ s in the ST diagram shown in Fig. 24. Note the source operating by a tail-instability mechanism next to the doublon.

2. *Interaction with subgrain boundaries*

The appearance of doublons above about $20 V_{CS}$ coincides with the fact that the pattern as a whole becomes unsteady (Fig. 24). In order to gain some insight into the

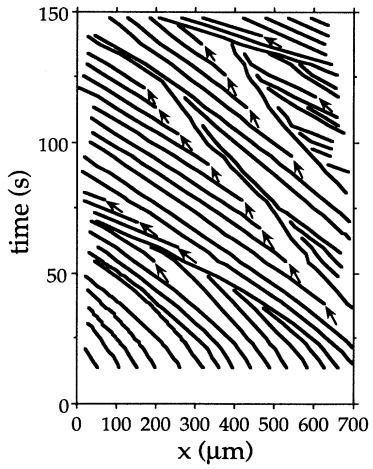

FIG. 24. Spatiotemporal diagram of the pattern shown in Fig. 23 ($V = 103\ \mu m\ s^{-1}$). The trajectories displayed are those of the (normal and SB) dendrite tips. The time $t = 0$ corresponds to the onset of the pulling. The duration of the initial transient is about 40 s. Arrows, creation of new dendrites by the tail-instability mechanism.

origin of this unsteadiness, we have carefully studied the long-time dynamics of the high-velocity regime. Unexpectedly, and contrary to seaweed patterns, this dynamics turns out to be controlled (or at least strongly influenced) by polygonization during growth. The investigation of the latter phenomenon is beyond the scope of this article, but it is necessary to briefly characterize its impact in order to establish that the observed coexistence between dendrites and doublons is intrinsic of the growth dynamics of the (perfect) crystal.

Initially, the grain considered here (Figs. 22–24) was a perfect single crystal. Four successive runs, separated by partial meltings, have been carried out on it, at $V \approx 8.4 V_{CS}$, $18 V_{CS}$, $54 V_{CS}$, and again $54 V_{CS}$. The successive stages of the initial transient of the first run at $V \approx 54 V_{CS}$ are shown in Fig. 22. The front at rest seems perfectly planar [Fig. 22(a)], but actually bears very shallow cusps, which were created during the run at $18 V_{CS}$. As could be expected, they are the sites where the destabilization of the planar front begins [Fig. 22(b)]. More unexpectedly, a doublon forms at each subgrain boundary in such a way that the subgrain boundary becomes attached to the inner groove of the doublon (and not to an outer groove). The nonuniform distribution of the subgrain boundaries along the front obviously leads to a heterogeneous structure. If the distance between the preexisting subgrain boundaries falls within the stable range of doublon spacings, a quasisteady pattern of doublons is formed; if not, dendrites (and perhaps also multiplets) appear [Fig. 22(d)].

The ST diagram in Fig. 24, together with the view of the growth front in Fig. 23, shows that the front is permanently divided in relatively wide subgrains whose boundaries are locked onto doublons. This is made apparent by the fact that the tilt angles of the dendrites on either side of a doublon are different from each other. It can also be seen that different doublons have different tilt angles, so that grains are continually eliminated. During this process, the average misorientation between grains is observed to increase.

The preceding analysis concerns crystals whose orientation is relatively close to (001)[100]. In such grains, we did not observe doublons without a subgrain boundary attached to their inner groove. So either doublons without subgrain boundaries are unstable or such doublons are stable, but their appearance depends on favorable initial conditions, which are, in the experiments, only provided by subgrain boundaries. Numerical simulations in directional solidification with a marked anisotropy ($\varepsilon = 0.12$) give a structure consisting of stable doublons at high velocity (see Sec. IV). Since these simulated finite-ε doublons do not reproduce the triangular shape of the experimental ones (which is certainly due to the predominance, in the experimental system, of kinetic anisotropy), this is not sufficient to remove all doubt about the possible intrinsic instability of experimental dendritic doublons. There are, however, additional hints in favor of the stability of the latter, in particular the fact that all subgrain boundaries give rise to doublons, whatever the sign of the misorientation. We therefore consider the intrinsic stability of dendritic doublons near the (001)[100] orientation as very likely. In any case, in more strongly misoriented grains, the stability of doublons is not doubtful, since they are created by tip splitting of large dendrites and are therefore free of subgrain boundaries (Fig. 3).

D. Crystals close to the degenerate {001}⟨110⟩ orientation

1. Degenerate pattern at low velocities

An interesting case of degeneracy is that of crystals presenting two equivalent minima of their $\tau(\alpha)$ plot arranged symmetrically relative to the pulling direction [15]. For a cubic crystal, this corresponds to the (001)[110] orientation. The major fact concerning such crystals is that an unsteady, strongly disordered regime, the degenerate regime, is found at low velocities. An example of it at $V \approx 3.7 V_{CS}$ is shown in Fig. 4. A numerical simulation in directional solidification performed with a $\tau(\alpha)$ plot corresponding to a perfect (001)[110] orientation is shown below in Fig. 31. The similarity with the observed patterns is striking.

The shape of the $\tau(\alpha)$ plot suggests to regard the degenerate pattern as resulting from a competition between embryos of three types of local structures, namely, dendrites tilted to the right, dendrites tilted to the left, and axial doublons. This view is only partly true. In fact, a specific local structure emerges out of the competition, which we call "tilted finger." The tilted finger shows some similarity with a tilted dendrite (it bears sidebranches on its external side), but definitely differs from it by the following features: (i) its tilt angle (about 23°, in absolute value, according to the numerical simulations) is much smaller than the one that dendrites would have at the same velocity (dendrites would run much closer to the ⟨100⟩ axes) and (ii) the trajectory of the tip is wavy and generally ends with a collision with a finger tilted in the opposite direction (the lifetime of the tilted fingers is long but finite).

2. Degenerate-to-dendrite and dendrite-to-dendrite transitions

The distinction between tilted fingers and dendrites is further confirmed by the transition from the degenerate pattern to a dendritic one observed as V increases. This degenerate-to-dendrite transition occurs slightly below $7 V_{CS}$. Above this threshold velocity, the front settles in one of the two possible steady dendritic modes. The transition is abrupt and reversible. No metastability of the two regimes is observed near the threshold velocity.

As V is further increased, in some crystals, the front is observed to undergo a second morphological transition from one to the other of the possible dendritic states (dendrite-to-dendrite transition). Figure 25 shows the same grain as in Fig. 4, at a higher velocity ($V \approx 17 V_{CS}$). In spite of appearance, this figure does not show a bicrystal, but a single crystal divided into two domains, one in the [100] dendritic state (prevalent at low V), the other in the [010] state (prevalent at high V). The competition be-

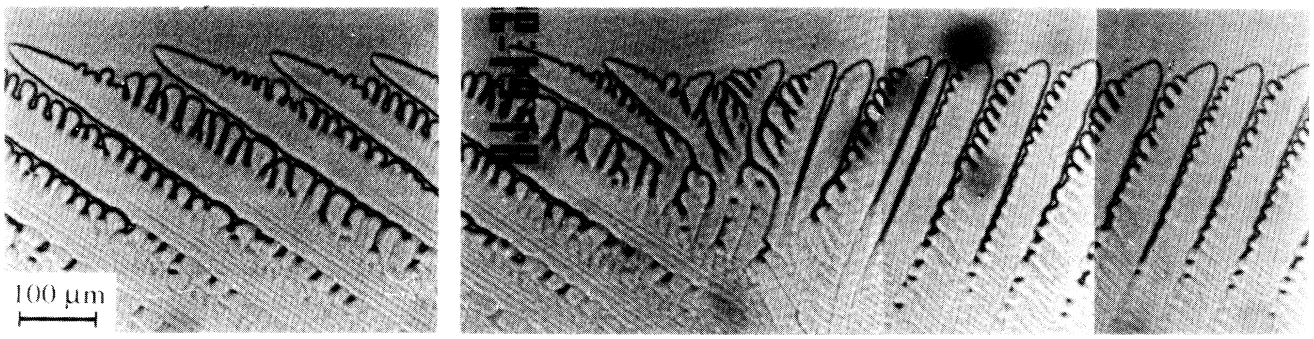

FIG. 25. Competition between two tilted dendritic states in a crystal close to the degenerate orientation (same crystal as in Fig. 4). $V=32\ \mu m\ s^{-1}$ ($\approx 17 V_{CS}$). Note the dynamic wall between two domains occupied by the [100] ($\phi \approx 22°$ to the right) and the [010] dendritic states ($\phi \approx 54°$ to the left), respectively.

tween the two states takes the form of an invasion of the front by the prevalent state (the [100] state). This and other observations not reported here clearly indicate that both dendritic states remain stable over a relatively large velocity range. Within this range, the outcome of the competition between the dendritic states at a fixed V is boundary-condition and history dependent.

Numerical simulations in directional solidification do not reproduce the degenerate-to-dendrite transition or the dendrite-to-dendrite one. It will be seen in Sec. IV that this discrepancy too can be attributed to the increasing kinetic effects as V increases in the experimental system.

E. Orientation dependence of the growth pattern

The above experimental results provide us with a number of indications about the types of growth patterns existing in our system, as a function of the orientation of the crystal at velocities much higher than V_c. Let us sum up this information by outlining stability diagrams of the system. A few preliminary words of caution about the transition lines appearing in such diagrams are necessary. We recall that the only transitions directly observable

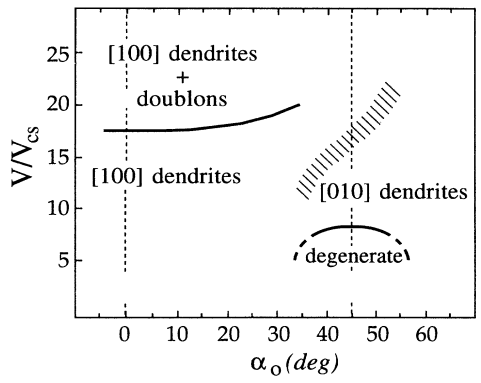

FIG. 26. Schematic diagram of the observed growth patterns as a function of the orientation of the crystal and the reduced pulling velocity. α_0, angle of rotation about the [001] axis. For $\alpha_0=0$, the orientation is (001)[100]. For $\alpha_0=45°$, it is approximately (001)[110] (a slight off-plane component of the misorientation is assumed, in order to make it possible to represent the dendrite-to-dendrite transition). Shaded region, cellular velocity range.

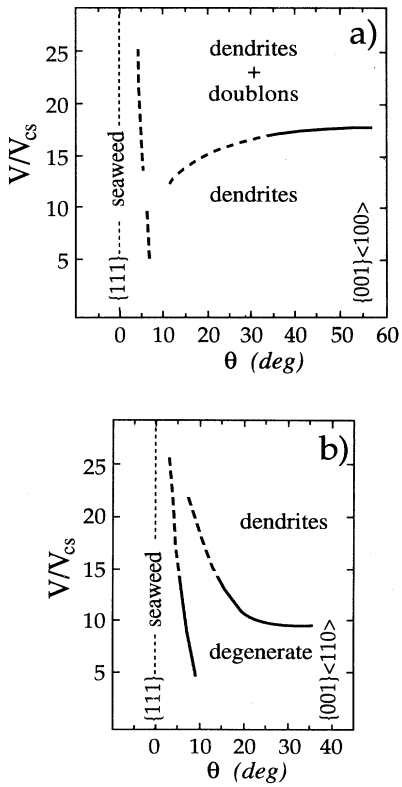

FIG. 27. Same type of diagrams as in Fig. 26, for a {111} initial orientation. θ, rotation angle. (a) Rotation towards a {001}⟨100⟩ orientation [a minimum of $\tau(\alpha)$ appears along the pulling direction as θ increases]; (b) rotation towards a {001}⟨110⟩ orientation [two minima of $\tau(\alpha)$ appear at $\pm 45°$ with respect to the pulling direction].

with our experimental setup are the transitions as a function of V, at fixed orientation. The transitions taking place as a function of the crystal orientation at fixed V have not been directly observed. We cannot be certain that these transitions do not involve some as yet unidentified intermediate types of pattern. In the diagrams below, the lines representing the transitions that have been directly observed are drawn in continuous lines, while those whose existence is only presumed are in dashed lines. It must also be understood that these diagrams are sketches, with no claim to accuracy.

Consider a (001)[100]-oriented crystal and assume that it can be rotated about the normal [001] to the plane of the film (such experiments have actually been performed by other authors [15,22,27]). The orientation variable is, in this case, the angle α_0 of the [100] axis with the pulling direction. The corresponding diagram is reproduced in Fig. 26. The major transitions are those corresponding to the appearance of dendritic doublons for orientations near (001)[100] at high V and the dendrite-to-degenerate transition near (001)[110] as α_0 is increased. Near this orientation also reproduced are the degenerate-to-dendrite and the dendrite-to-dendrite transitions as V increases at fixed α_0.

Figure 27 shows the transitions occurring as the misorientation from a (111)-oriented crystal increases. Figure 27(a) corresponds to a rotation of the crystal leading to a standard $\{001\}\langle 100\rangle$ orientation. As the misorientation increases, a minimum of $\tau(\alpha)$ appears along the pulling direction and grows in amplitude. In this case, the noteworthy morphological transitions are the seaweed-to-dendrite transition and, as in Fig. 26, the appearance of dendritic doublons at high velocity near the $\{001\}\langle 100\rangle$ orientation.

Figure 27(b) corresponds to a rotation of the (111)-oriented crystal leading to a degenerate $\{001\}\langle 110\rangle$ orientation. In this case, two minima of $\tau(\alpha)$ appear at $\pm 45°$ with respect to the pulling direction as the misorientation increases. The transitions displayed are the seaweed-to-degenerate and the degenerate-to-dendrite transitions (for simplicity the dendrite-to-dendrite transition is not represented). The diagram takes into account the fact that the seaweed-to-degenerate and the degenerate-to-dendrite transitions are sometimes observed to occur as V increases at fixed α (which we attribute to kinetic effects).

IV. NUMERICAL RESULTS

A. Model and methods

For the simulation of 2D directional solidification, we used the so-called one-sided diffusion model [2,3]

$$\frac{\partial}{\partial t}u(x,y,t)=D\nabla^2 u(x,y,t) , \tag{6}$$

$$u_s=1-d(\alpha)\kappa-\frac{y-Vt}{l_{\rm th}} , \tag{7}$$

$$\{K+(1-K)u_s\}v_n=-D\mathbf{n}\cdot\nabla u , \tag{8}$$

where $u(x,y,t)$ is the normalized concentration field (see Fig. 5 for the definition of axes), which obeys the diffusion equation (6) for the solute in the liquid phase. We are solving here the fully time-dependent diffusion equation (i.e., without the quasistationary approximation [28]), which allows us not only to find stable stationary states, but also to follow the real-time dynamical evolution. It yields, for example, the possibility of identifying oscillatory behaviors.

Equation (7), where κ is the local curvature, is the Gibbs-Thomson condition of local equilibrium. At $y=\infty$, one has $u=0$. The anisotropic capillary length d, which is proportional to the surface stiffness τ [see Eq. (5)], is assumed here to have a fourfold symmetry as

$$d(\alpha)=d_0\{1-\varepsilon\cos 4(\alpha-\alpha_0)\} , \tag{9}$$

where ε and α_0 have the same meaning as above. The frame of reference is moving at the pulling velocity V, which leads to the explicit time dependence in the boundary condition (7). Equation 8, in which v_n is the normal velocity and $\mathbf{n}$ the normal vector of the moving boundary, is the conservation law for the solute at the interface.

For comparison with previous simulations, we define the time-dependent tip undercooling Δ

$$\Delta(t)=1-\frac{y_{\rm tip}(t)-Vt}{l_{\rm th}} , \tag{10}$$

$y_{\rm tip}$ being the position of the foremost point (tip) of a local structure. If the structure is stationary, the growth velocity of this tip is equal to the pulling velocity V and Δ is therefore constant. As defined, $\Delta=1$ for the steady planar front.

Let us first consider the transposition of the results already obtained in free growth [7,8] to the case of directional solidification. In the limit of large thermal length $l_{\rm th}\gg l_d$ (or, equivalently, $V\gg V_{\rm CS}$), the stationary structures obtained in directional solidification are approximately the same as in free growth, at least in the tip region. This is supported by numerical simulations by Saito, Misbah, and Müller-Krumbhaar [23] showing that, in directional solidification at $l_{\rm th}\approx 15 l_d$, dendrite tips fulfill the same scaling relations as in free growth within a few percent.

Furthermore, provided that Δ is sufficiently small, it is possible to define a transformation that gives the selection rules for any value of the segregation coefficient K, knowing those valid for $K=1$. Let us focus on the case of dendrites and define the Péclet number Pe as a function of Δ by the Ivantsov relation:

$$\Delta=2\sqrt{\rm Pe}\,e^{\rm Pe}\int_{\sqrt{\rm Pe}}^{\infty}dx\,\exp(-x^2) . \tag{11}$$

The condition that Δ is small can be specified as $\mathrm{Pe}(\Delta)<1$. As a first step, one approximates the flux condition (8) by

$$\{K+(1-K)\Delta\}v_n=-D\mathbf{n}\cdot\nabla u , \tag{12}$$

which should hold in the tip region since $u_{\rm tip}=\Delta-d_0/R_{\rm tip}=\Delta-\mathrm{Pe}\,\sigma\approx\Delta$, where $\sigma(\varepsilon)=d_0 v/(2D\,\mathrm{Pe}^2)$ is of the order of 0.05. The small temperature gradient ensures that Δ is almost constant over the tip re-

gion like in free growth. Then the diffusion field u is rescaled by

$$\tilde{u}=\frac{u}{K+(1+K)\Delta} . \tag{13}$$

For this new field $\tilde{u}$, the boundary conditions for free growth (with $K=1$) are

$$\tilde{u}_s=\tilde{\Delta}-\tilde{d}_0\kappa , \tag{14}$$

$$v_n=-D\mathbf{n}\cdot\nabla\tilde{u} , \tag{15}$$

where the rescaled undercooling $\tilde{\Delta}$ and capillary length $\tilde{d}_0$ are defined as

$$\tilde{\Delta}=\frac{\Delta}{K+(1-K)\Delta} , \tag{16}$$

$$\tilde{d}_0=\frac{d_0}{K+(1-K)\Delta} . \tag{17}$$

This is the desired transformation.

To solve numerically the Stefan problem defined by Eqs. (6)–(8), we used the same method as the one previously used for free growth by one of the authors [7], except for small differences in the boundary conditions (7) and (8). The method is described in detail in Ref. [7] and we shall only mention some basic features here.

First, the solid-liquid interface is handled explicitly, i.e., the interface is discretized and represented by a set of points. The two-dimensional diffusion field u is discretized too on a simple square grid. After setting initial values for the interface position as well as for the diffusion field, a diffusion step is performed by means of the discretized version of the diffusion equation (6):

$$u_{i,j}^{n+1}=u_{i,j}^{n}+\frac{D\Delta t}{\Delta x^2}(u_{i+1,j}^{n}+u_{i-1,j}^{n}+u_{i,j+1}^{n}+u_{i,j-1}^{n}-4u_{i,j}^{n}) \tag{18}$$

with a small time step $\Delta t<(\Delta x)^2/(4D)$, where Δx is the lattice unit of the diffusional grid. Then the gradient of the new diffusion field is determined at the interface and each point of the discretized interface is advanced by the distance $v_n\Delta t$ according to Eq. (8). After that, the boundary condition (7) has to be incorporated into the diffusion field. The whole procedure is then repeated beginning with the diffusion step and so on. The moving interface is always kept approximately at the center of the lattice, which allows us to follow the growth over any distance. The distance between the moving front and the end of the periodic channel far inside the liquid is at least five diffusion lengths, in order to keep the growth unaffected by boundary effects.

Since anisotropy is an important parameter for the selection of dendrites, the artificial anisotropy introduced by the square diffusional lattice has to be reduced. Therefore, two or four independent diffusion lattices are used that are rotated and shifted against each other. In each time step, the diffusion equation is solved independently on all lattices. We then locally advance the moving boundary independently on all lattices and average the resulting new boundary position over all lattices. For free dendritic growth it was shown that this averaging is crucial at small anisotropy. For example, at $\varepsilon\approx 0.05$, if this averaging is not applied, the velocity of the dendrites is found to be artificially increased by a factor of 2.

Nine simulations in directional solidification have been performed. The corresponding parameters and some numerical results are listed in Table IV. These simulations did not include any kinetic coefficient or kinetic anisotropy, which in principle can be easily done [11,29], but would introduce two additional unknown parameters. Since the CPU time for one run is of the order of 5–15 h on a Cray-YMP computer, a scanning through this parameter space seems not reasonable and we restricted ourselves to the purely capillary case. In all the simula-

TABLE IV. Parameters and results of nine numerical simulations performed in directional solidification. N, number of grids used; W, width of the inner groove of doublons (see the text for the definitions of the other symbols). Lengths are given in units of the grid spacing Δx and velocities in units of $D/\Delta x$ (in these units, $V/V_{CS}\equiv Vl_{th}$). For columns 3–9, the value of Δx in μm can be calculated knowing that $d_0=0.054$ μm (Table II). In columns 3–6, $l_{th}=200$ μm is somewhat smaller than in Table II, but the difference falls into the experimental margin of error.

Parameter	1	2	3	4	5	6	7	8	9
K	0.9	0.9	0.75	0.75	0.75	0.75	0.75	0.75	0.75
d_0	0.1237	0.1237	0.135	0.108	0.135	0.0864	0.8	0.8	0.8
ε	0.1	0.1	0.12	0.12	0.12	0	0	0.1	0.12
α_0	0	0	0	36°	45°	0	0	0	0
l_{th}	419.4	419.4	500	400	500	320	987.6	987.6	987.6
V	0.0286	0.047 68	0.0256	0.032	0.0256	0.04	0.035	0.043 75	0.05
V/V_{CS}	12	20	12.8	12.8	12.8	12.8	34.6	43.2	49.4
L	151	151	997	635	997	471	460	460	460
N	4	4	2	2	2	2	4	4	4
Δ	0.599	0.613	0.516	0.571	0.60	0.50	0.6671	0.6678	0.675
R	19.05	15.10	16.6	12.0		12.0	31.2	25	23.5
W						11.2	19.7	21.3	20.6

tions, periodic boundary conditions at the sides of the channel and mostly two diffusional grids are used, rotated by an angle of $\pi/4$ against each other.

B. Results

1. Axial dendrites

In order to check our numerical code, we first attempted to reproduce the results obtained by Saito, Misbah, and Müller-Krumbhaar [23] for directional dendritic growth in a channel with a quasistationary Green's function method. The dimensionless parameters used there were $D=1$, $l_{th}=1$ (entailing $V_{CS}=1$), $K=0.9$, $d_0=0.000\,295$, and $L=0.36$, the resulting critical velocity and wavelength for the plane front instability being $V_c=1.136$ and $\lambda_c=0.514$. The anisotropy of the capillary length was $\varepsilon=0.1$. In the spacing units of the diffusional grid Δx, we chose $l_{th}=419.44\Delta x$ and rescaled all other lengths (channel width L, diffusion length l_d, capillary length d_0) with the same factor, the diffusion constant D remaining equal to 1.

As in Ref. [23], we performed two simulations (columns 1 and 2 in Table IV) at $V/V_{CS}=12$ and 20, starting with an almost flat interface slightly perturbed by one period of a cosine and an exponential decaying diffusion field as initial conditions. In the first run, the final stationary dendrite has a tip undercooling of $\Delta=0.599$ and a tip radius $R=19.05$ (in lattice units). The corresponding values from the Green's function simulation [30] are $\Delta=0.584$ and $R=17.33$. In the second run we measured $\Delta=0.613$ and $R=15.1$, to be compared with $\Delta=0.573$ and $R=12.2$ obtained by the Green's function method. The two sets of results agree within 20%.

Our fully dynamic method allows us to find that the initial transient towards the stationary state consists of a damped oscillatory behavior of the tip undercooling and velocity (see also below). The damping of the oscillations is strong—only two periods are visible—but we can estimate the period to be $16.4\tau_d$ in the first run and $20.7\tau_d$ in the second. Unlike in free growth, where this convergence is poorly relaxational, dendrites in directional solidification have to choose the right position in the sample, i.e., the right tip undercooling, in order to become stationary. Therefore we believe that this additional constraint leads to this new time scale.

The next step is now to introduce parameters corresponding to the experiments in the simulations. Except for ε, the values used in the calculation are those given in Tables I and II. The value $\varepsilon=0.12$ was chosen because, using the theory of free dendrites [2,3], it gives the same value of the tip radius of the steady dendrites as the one measured in Sec. III A. Figure 28 shows the final steady state of an array of five axial dendrites ($\alpha_0=0$) corresponding to $\varepsilon=0.12$, $K=0.75$, and $V/V_{CS}\approx 13$ (column 3 in Table IV). The channel width is $L=997$ and the period of the initial sinusoidal perturbation is $\lambda=199.4$ ($\approx 51_d$), imposing the primary spacing of the five dendrites in the channel (the primary spacing corresponds to 80 μm, which belongs to the stable experimental range of spacings). The tip radius of the dendrites is 16.6 internal units. This would correspond to 6.6 μm in reality, which is quite close to the measured value of 7.0 ± 0.5 μm in Table III.

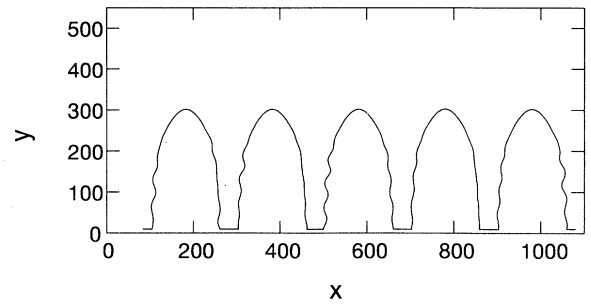

FIG. 28. Steady state of an array of five axial dendrites at $\varepsilon=0.12$. $l_d=39\Delta x$, corresponding to 15.6 μm in experiment (see column 3 in Table IV). Here and in the following figures, all lengths are given in units of the diffusional grid Δx and all times are measured in units of $\Delta x^2/D$.

The oscillatory relaxation of the tip undercooling to its stationary state is again found (Fig. 29), with a period of about $17.4\tau_d$. In our experiments, this initial oscillation of the homogeneous pattern cannot be observed, being hidden by the transient of instrumental origin described in Sec. II. However, we observed a similar, strongly damped oscillation of the tip of dendrites newly created by a tail instability, with a period of about $10\tau_d$, the amplitude of the oscillation being highly grain dependent.

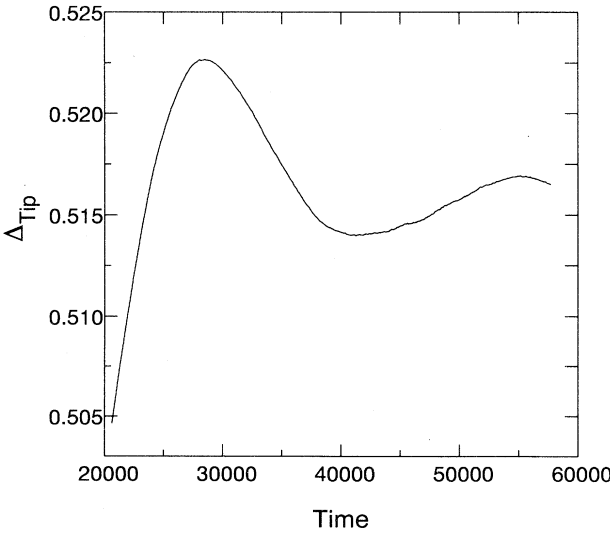

FIG. 29. Time evolution of the reduced tip undercooling $\Delta_{tip}=1-(y_{tip}-Vt)/l_{th}$ for the dendrites of Fig. 28.

2. Tilted dendrites and degenerate pattern

Next, we investigated the case of an array of four tilted dendrites. The physical parameters are the same as before except that the angle α_0 between the growth axis and the $\langle 100 \rangle$ direction is different from zero (column 4 in Table IV). The initial condition is a small asymmetric perturbation with four periods. The final steady state is given in Fig. 30. We find that, at these values of the parameters, tilted dendrites are stable only if α_0 does not exceed $\alpha_{\text{crit}} \approx 36°$, and this, independently of the spacing of the dendrites. The resulting tilt angle ϕ of the dendrites—measured here by means of the tilt of the grooves between them—is always smaller than α_0, like in experiments (it is about 30° at $\alpha_0 = 36°$).

The instability of the dendrites for $\alpha_0 > 36°$ is clearly due to the competition between the tip of each dendrite and the first sidebranch of its preceding neighbor. Figure 31 shows the spatiotemporal plot of the pattern obtained in the case $\alpha_0 = 45°$ (column 5 in Table IV). As announced in Sec. III D, this pattern is strikingly similar to the degenerate pattern experimentally observed in nearly $\{001\}\langle 110 \rangle$-oriented crystals. It mainly consists of competing right and left tilted finger, whose average tilt angle is about 23°, thus significantly smaller than the maximum angle reached by the tilted dendrites ($\approx 30°$ at $\alpha_0 = 36°$). The average undercooling at the front in the degenerate pattern is $\Delta = 0.6$, noticeably higher than at the tips of the dendrites ($\Delta = 0.516$).

Since, in the simulations, sidebranching appears to be responsible for the instability of dendrites for $\alpha_0 > 36°$, the fact that, in the experiments, stable tilted dendrites are observed for α_0 as large as 55° is certainly due to the strong reduction of the amplitude of the sidebranches by kinetic effects [11]. This, of course, suggests that the degenerate-to-dendrite and dendrite-to-dendrite transitions described in Sec. III D2 are manifestations of the increasing importance of kinetic effects as V increases. This, however, has not been proven yet.

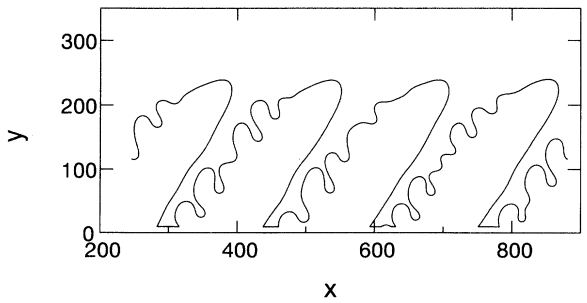

FIG. 30. Final state of four tilted dendrites (see column 4 in Table IV). Same conditions as in Fig. 28, except that the angle between the fourfold symmetry axis and the pulling direction is $\alpha_0 = 36°$. The tilt of these dendrites is about 30°. $l_d = 31.25\Delta x$.

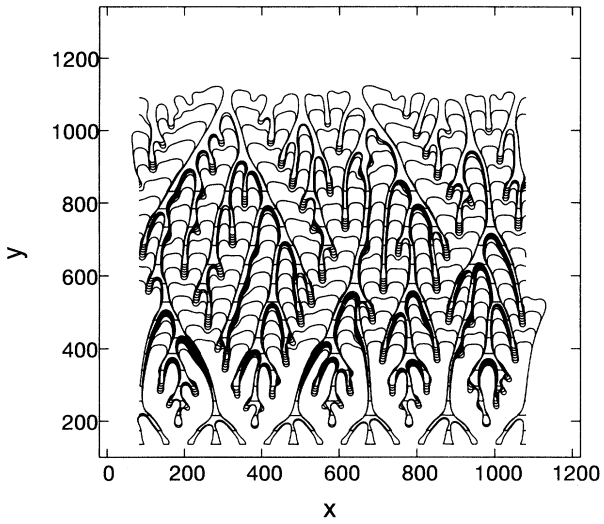

FIG. 31. Time sequence of the degenerate pattern. Same conditions as in Fig. 28, except that $\alpha_0 = 45°$ (see column 5 in Table IV). The tilted fingers in this pattern have an average tilt angle of about 23°. $l_d = 39\Delta x$.

3. Doublons

Doublons at $\varepsilon = 0$ have been already numerically investigated in free growth with $K = 1$ (see Fig. 1) [7]. This investigation showed that, like dendrites, doublons obey selection rules. The dependence of their velocity V and the width of their inner groove W on undercooling at $\varepsilon = 0$ is shown in Figs. 32(a) and 32(b), respectively. With the transformation defined in Eqs. (16) and (17) in hand, these predictions can be compared to the experimental measurements performed in $\{111\}$-oriented grains. Concerning the dependence of W on V, the comparison is done in Fig. 16. It can be seen that the calculated width is about twice as large as the experimental data, which can be considered as a satisfactory agreement between simulations and experiments, knowing, in particular, that the 3D deformations of experimental patterns are noticeable (W is much smaller than the film thickness). Concerning the value of Δ, the agreement is satisfactory too (see Sec. III B 1).

Let us now turn to the simulations in directional solidification at $\varepsilon = 0$. Two runs at $V/V_{\text{CS}} \approx 13 V_{\text{CS}}$ and $35 V_{\text{CS}}$ are shown in Figs. 33 and 34, respectively (columns 6 and 7 in Table IV; for efficiency purposes, the run at $35 V_{\text{CS}}$ is performed with a much smaller l_{th} value than in the experiments). The structure obtained at $35 V_{\text{CS}}$ clearly consists of quasisteady doublons. At $13 V_{\text{CS}}$, the differentiation between wide and narrow grooves is less pronounced, but asymmetric fingers, associated in pairs, can nevertheless be seen. The tip undercooling at this velocity is $\Delta = 0.5$, which is consistent with the selection rules for doublons reproduced in Fig. 32 (according to Eq. (13), $\tilde{\Delta} = 0.57$; similarly, the reduced values of V and W are $\tilde{V} = V d_0 / D[K$

$+(1-K)\Delta]=0.003\,95$ and $\tilde{W}=W[K+(1-K)\Delta]/d_0=113$). So, like in the experiments in {111}-oriented crystals, the growth patterns at $\varepsilon=0$ essentially consist of doublons. Moreover, like in the experiments, no hint of stationarity is observed in the simulations. On the other hand, the correspondence between the experimental and numerical velocity scales is not perfect. The numerical pattern at $13V_{CS}$ resembles the experimental pattern at $5V_{CS}$ [Fig. 10(a)]. There are several possible origins of this discrepancy: the above-mentioned 3D effects, a possible remnant anisotropy in the {111} planes of the crystal, the possible kinetic nature of the latter, and the experimental uncertainty on the value of the physical parameters of the material. Which of these effects is relevant can only be determined by further numerical simulations.

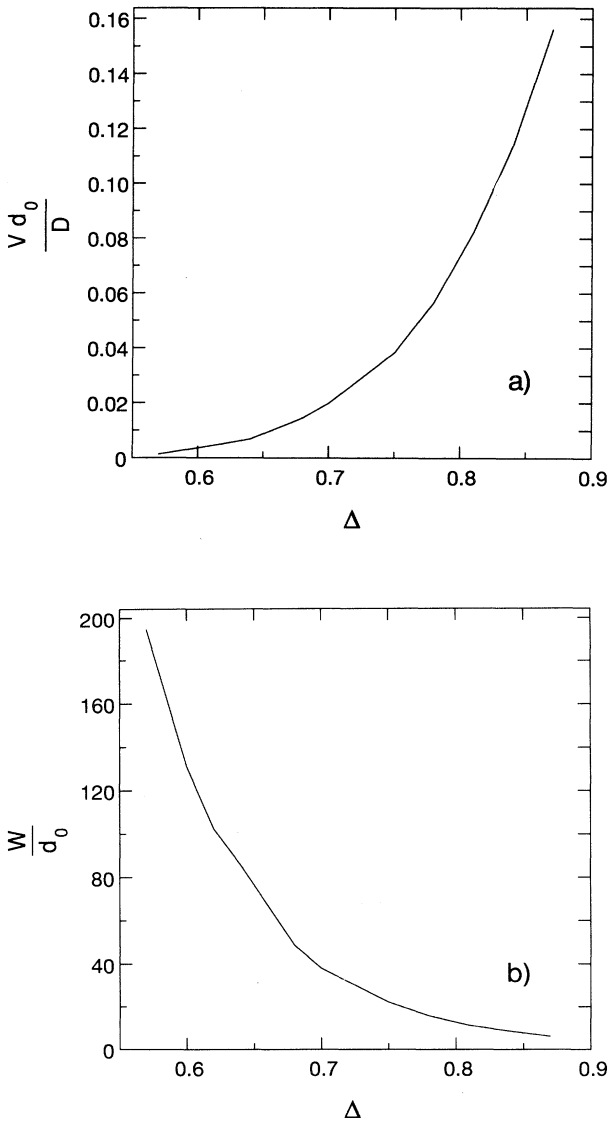

FIG. 32. (a) Normalized velocity of doublons vs undercooling obtained in free growth simulations at $\varepsilon=0$ in an extended system [7]. (b) Width of the inner groove of doublons in units of the capillary length d_0.

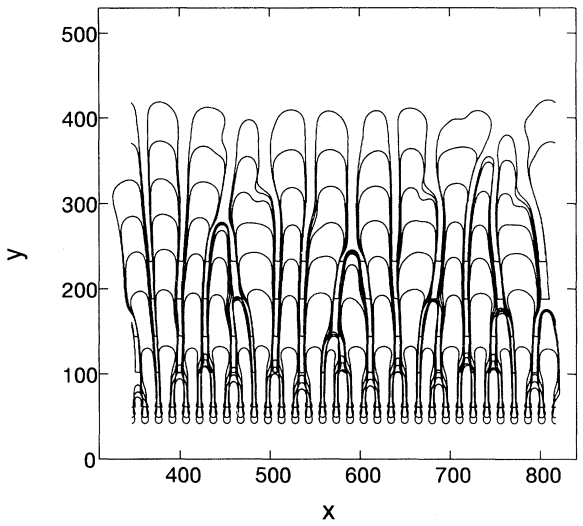

FIG. 33. Time evolution of a system at $\varepsilon=0$ and $V\approx 13V_{CS}$. The other physical parameters are the same as in Fig. 28 (see column 6 in Table IV). $l_d=25\Delta x$ corresponding to 15.6 μm.

Finally, we looked for the doublon structure at strong anisotropy. According to theory, this should be possible in free growth at very high undercooling $\Delta\approx 0.8$, thus, in

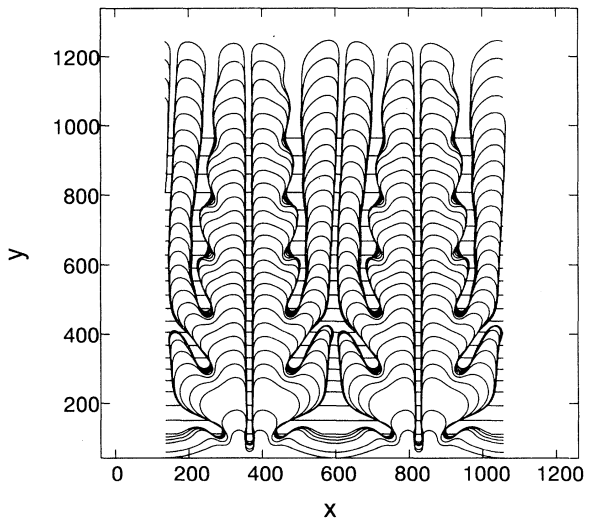

FIG. 34. Doublons at $V\approx 35V_{CS}$ and $\varepsilon=0$ (see column 7 in Table IV). For numerical efficiency the physical parameters correspond here to an unrealistic experiment with a very high velocity (259 μm s^{-1}) and a small thermal length ($l_{th}=66.7$ μm). $l_d=1.93$ μm, corresponding to $28.6\Delta x$. Note that, contrary to previous figures, two periods of the structure are plotted ($L=460$).

directional solidification, at a high pulling velocity. For ε values of 0.1 and 0.12, we found stable doublons for $V=43.2V_{CS}$ and $49.4V_{CS}$ (columns 8 and 9 in Table IV). The shape of these "finite-ε" doublons, quite similar to that of "zero-ε" doublons, is not reproduced here. The transition from dendrites to doublons at large velocity in strongly anisotropic crystals is also observed experimentally, as explained in Sec. III C. The difference of shape between finite-ε and zero-ε doublons noted in the experiments is not reproduced numerically and can again be attributed to kinetic anisotropy.

V. CONCLUSION

We presented above a detailed experimental and numerical investigation of the growth patterns in thin-film directional solidification of the CBr_4–8 mol % C_2Cl_6 alloy, as a function of the orientation of the crystal with respect to the solidification setup. The following results can be considered as firmly established thanks, in particular, to the good agreement between experimental observations and numerical simulations.

(i) When a $\{111\}$ plane of the crystal is parallel to the plane of the sample, the effective crystal anisotropy is sufficiently low for the growth front to assume a nondendritic unsteady pattern, which we identify as the seaweed morphology consisting of doublons, recently revealed by numerical simulations in free growth at zero and weak anisotropy [7]. Spatiotemporal diagrams show that the seaweed pattern is divided into quasistationary seaweed cells (typically $5l_d$ wide), separated by long liquid grooves. These cells have an internal dynamics consisting of a continual creation and elimination of doublons. We thus confirm that the doublon is the basic building block of this pattern and moreover show that its characteristic dimensions and undercooling at the tip are well-defined functions of growth velocity. The inner groove of constant, small width (typically 0.21_{ld}) acts as an identifying feature for this morphology. On the other hand, the growth direction of doublons is not selected, but determined by initial conditions (as expected from the fact that the stability of doublons does not arise from crystal anisotropy).

(ii) Dendritic doublons (i.e., pairs of symmetry-broken dendrites) exist at high pulling velocities ($V>20V_c$), in crystals presenting a $\langle 100\rangle$ axis nearly parallel to the pulling axis, i.e., crystals with a strong effective anisotropy. These finite-ε doublons coexist with dendrites. In crystals very close to $\{001\}\langle 100\rangle$, they are created by pairing of dendrites, which is compatible with previous numerical simulations, showing that the stability of doublons against unbinding into single dendrites weakens when the anisotropy increases. In crystals with a relatively large misorientation with respect to $\{001\}\langle 100\rangle$, doublons are created by tip splitting.

(iii) In crystals presenting two $\langle 100\rangle$ axes symmetrically arranged with respect to the pulling axis, we observe an unsteady, nondendritic pattern of a different nature from the seaweed pattern. This degenerate pattern is essentially made of competing fingers tilted at about $\pm 23°$ with respect to the pulling axis.

Other points of interest remain partly unclear.

(iv) There is little doubt that the instability of doublons against tilting (or, in other words, the fact that their growth direction is not selected) plays a major part in the unsteadiness of the seaweed pattern. This, however, does not explain (i) the fact that the transition from unstable to stable doublons found in numerical simulations in free growth [26] is not observed experimentally, (ii) the robustness of the seaweed cells against the instability of their internal structure, (iii) the values of the bounds of the spacing distribution of the seaweed cells, and (iv) the role played by transient multiplets. A study of the low-velocity regimes in $\{111\}$-oriented crystals, currently in progress, will probably cast more light on this subject.

(v) Some discrepancies of limited importance between experiments and simulations are attributable to 3D deformations of the growth front and polygonization during growth. A more essential source of discrepancy is the presence, in the CBr_4-C_2Cl_6 system, of a marked kinetic-coefficient anisotropy (not taken into account in the simulations), which is revealed by the triangular shape of the dendrite tips and the reduced amplitude of the sidebranches in nearly $\{001\}\langle 100\rangle$-oriented crystals. In crystals oriented close to the degenerate $\{001\}\langle 110\rangle$ orientation, a transition from the degenerate pattern to a tilted dendritic pattern (of tilt angle close to 45°) is observed at $V\approx 7V_{CS}$ and another transition from the latter to the other possible tilted dendritic pattern (tilted at about 45° in the other direction) is found at $V\approx 17V_{CS}$. These transitions cannot be reproduced by simulations without kinetic effects since, in the latter, dendrites tilted to an angle higher than about 30° are unstable, being destroyed by their interaction with the sidebranches of their neighbors. The stability of such dendrites in the experimental system is thus likely to be due to the suppression of the sidebranches by kinetic effects. This is a necessary, but not sufficient, condition for the occurrence of the degenerate-to-dendrite and dendrite-to-dendrite transitions at high velocities. We hope to report more precisely on the role played by kinetic anisotropy in such transitions in the near future.

ACKNOWLEDGMENTS

This study was initiated thanks to an occasional observation of a seaweed pattern in CBr_4-C_2Cl_6 alloy by M. Ginibre. We thank her for having drawn our attention to this finding. We gratefully acknowledge many stimulating discussions with H. Müller-Krumbhaar and C. Caroli. Some discussions with A. Karma and W. van Saarloos were also illuminating. Thanks are also due to R. Mellet and A.-M. Pougnet, of the Centre National d'Etudes des Télécommunications, France-Telecom, Bagneux, France, for providing us with zone-refined chemicals. The experimental part of this study was financially supported by the Centre National d'Etudes Spatiales, France.

APPENDIX

It is common practice to expand the functions invariant with respect to the symmetries of the cube in cubic

spherical harmonics of increasing order (H_n). This expansion is the analog, for two angular variables, of a Fourier series for one variable. The first nonconstant term is the fourth-order harmonic, which is, up to a constant, proportional to the function $f_4(\mathbf{n})$ defined in Eq. (2). It is easily verified that a Wulff plot described by $f_4(\mathbf{n})$ has its maxima and minima in the $\langle 100 \rangle$ and $\langle 111 \rangle$ directions, respectively, and saddle points in the $\langle 110 \rangle$ directions. Its cross sections by the $\{111\}$ planes are circles. In other words, $\gamma(\mathbf{n})$ as given by Eq. (3) is the same for all the orientations of $\mathbf{n}$ belonging to the $\{111\}$ planes. This can be directly checked by a simple calculation ($f_4 \equiv 0.5$ if $|n_1|+|n_2|+|n_3|=0$) or deduced from a general symmetry argument (the threefold symmetry in a $\{111\}$ plane can only be ensured by powers of the n_i's multiple of 3). To a higher order, the cross sections of the Wulff plot by the $\{111\}$ planes would not be circular, but present a modulation with a sixfold symmetry.

In the absence of direct knowledge of the physical properties of the solid-liquid interface, it is natural to take $f_4(\mathbf{n})$ as a tentative description of their orientation dependence [31]. Assuming that $\gamma(\mathbf{n})$ varies as $f_4(\mathbf{n})$, it is a matter of elementary geometry to calculate the functions $\gamma(\alpha)$ and $\tau(\alpha)$ for any orientation of the crystal with respect to the solidification setup. In general, the Fourier series of these functions contain terms in $\cos(2\alpha)$ and $\cos(4\alpha)$. It is convenient to put the expansions in the form

$$\gamma(\alpha)=\gamma_0\left\{1+\frac{\varepsilon}{15}[5\beta_2\cos 2(\alpha-\alpha_0-\alpha_2)+\cos 4(\alpha-\alpha_0)]\right\}, \tag{A1}$$

$$\tau(\alpha)=\tau_0\{1-\varepsilon[\beta_2\cos 2(\alpha-\alpha_0-\alpha_2)+\cos 4(\alpha-\alpha_0)]\}, \tag{A2}$$

In these expressions, τ_0, ε, β_2, and α_2 are functions of the orientation of $\mathbf{z}$ (normal to the thin film) relative to the crystal, while α_0 is a function of the orientation of $\mathbf{y}$ (the pulling axis). The $\mathbf{z}$ dependence of τ_0 is negligible if $\varepsilon_M \ll 1$. If $\mathbf{z}=\langle 001 \rangle$, ε takes its maximum value ε_M.

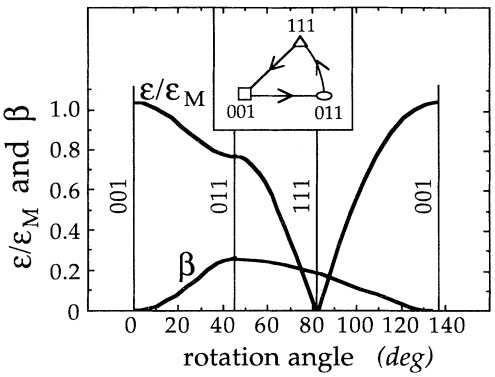

FIG. 35. Parameters $\varepsilon/\varepsilon_M$ and β_2, defined in Eq. (A3), describing the 2D anisotropy as a function of the orientation of the normal to the plane of the thin film (z) with respect to the crystal. Inset: trajectory of z represented in stereographic projection.

For a given orientation, the quantity of interest is not $\tau(\alpha)$ itself, but its normalized anisotropic component defined as

$$\frac{\tau(\alpha)-\tau_0}{\varepsilon_M}=-\frac{\varepsilon}{\varepsilon_M}[\beta_2\cos 2(\alpha-\alpha_0-\alpha_2)+\cos 4(\alpha-\alpha_0)], \tag{A3}$$

which is equal to $\cos(4\alpha)$ in the (001)[100] orientation.

The dependence of β_2 and $\varepsilon/\varepsilon_M$ on the orientation of the normal to the thin film is represented in Fig. 35. It can be seen that β_2 is small compared to 1 in the vicinity of the (001)[100] orientation. In this region of the orientation space, it is admissible to neglect the term in $\cos(2\alpha)$. This leads to Eq. (5) in the text. It is also worth noting that $\varepsilon/\varepsilon_M$ is of order 1 for all orientations, except for those very close to (111), in agreement with the observed fact that the seaweed pattern is only observed for misorientations from the perfect (111) orientation smaller than a few degrees.

[1] J. S. Langer, in *Chance and Matter,* edited by J. Souletie, J. Vannimenus, and R. Stora (Elsevier, Amsterdam, 1987).
[2] D. A. Kessler, J. Koplik, and H. Levine, Adv. Phys. **37**, 255 (1988).
[3] H. Müller-Krumbhaar and W. Kurz, *Phase Transformation in Materials,* edited by P. Haasen (VCH-Verlag, Weinheim, 1991).
[4] Y. Pomeau and M. Ben Amar, in *Solids far from Equilibrium,* edited by C. Godrèche (Cambridge University Press, Cambridge, England, 1992).
[5] E. Ben-Jacob, G. Deutscher, P. Garik, N. D. Goldenfeld, and Y. Lareah, Phys. Rev. Lett. **57**, 1903 (1986); E. Ben-Jacob, P. Garik, T. Müller, and D. Grier, Phys. Rev. A **38**, 1370 (1988).
[6] P. Oswald, J. Malthête, and P. Pelcé, J. Phys. (Paris) **50**, 2121 (1989).
[7] T. Ihle and H. Müller-Krumbhaar, Phys. Rev. Lett. **70**, 3083 (1993); Phys. Rev. E **49**, 2972 (1994).
[8] E. Brener, H. Müller-Krumbhaar, Y. Saito, and D. Temkin, Phys. Rev. E **47**, 1151 (1993).
[9] E. A. Brener, H. Müller-Krumbhaar, and D. E. Temkin, Europhys. Lett. **17**, 535 (1992).
[10] R. Kupfermann, D. A. Kessler, and E. Ben-Jacob Physica A **213**, 451 (1995).
[11] A. Classen, C. Misbah, H. Müller-Krumbhaar, and Y. Saito, Phys. Rev. A **43**, 6920 (1991).

[12] M. Rabaud, Y. Couder, and S. Michalland, Eur. J. Mech. B **10**, 253 (1991).

[13] H. Jamgotchian, R. Trivedi, and B. Billia, Phys. Rev. E **47**, 4313 (1993).

[14] Dendrites with a split tip were observed, for instance, in ice crystals by K. K. Koo, R. Ananth, and W. N. Gill, Phys. Rev. A **44**, 3782 (1991), and in a discotic liquid crystal by J. C. Géminard, thèse de doctorat, Université Lyon 1, 1993.

[15] F. Heslot and A. Libchaber, Phys. Scri. **T9**, 126 (1985).

[16] K. A. Jackson and J. D. Hunt, Acta Metall. **13**, 1212 (1965).

[17] J. Mergy, G. Faivre, C. Guthmann, and R. Mellet, J. Cryst. Growth **134**, 353 (1993); see also G. Faivre and J. Mergy, Phys. Rev. A **45**, 7320 (1992); **46**, 963 (1992). A detailed account of the role of residual gases, gas bubbles, and 3D deformations of the growth front in our experiments will be given in a forthcoming paper by S. Akamatsu and G. Faivre.

[18] G. Grange, C. Jourdan, J. Gastaldi, and B. Billia, J. Phys. (France) III **4**, 293 (1994), and private communication.

[19] A. Pavlovska and D. Nemow, J. Cryst. Growth **39**, 346 (1977). These authors found that the gas inclusions at rest have large {111} facets and small {100} facets. We find here that the main facets are {100}, which may stem from the fact that we are observing growth (and not equilibrium) facets.

[20] W. A. Tiller, J. Appl. Phys. **34**, 2757 (1963).

[21] R. Trivedi, Appl. Mech. Rev. **43**, S79 (1990); R. Trivedi, V. Seetharaman, and M. A. Eshelman, Metall. Trans. **22A**, 585 (1991).

[22] P. Oswald, M. Moulin, P. Metz, J. C. Géminard, P. Sotta, and L. Sallen, J. Phys. (France) III **3**, 1891 (1993).

[23] Y. Saito, C. Misbah, and H. Müller-Krumbhaar, Phys. Rev. Lett. **63**, 2377 (1989).

[24] R. Trivedi, J. A. Sekhar, and V. Seetharaman, Metall. Trans. **20A**, 769 (1989).

[25] P. Kurowski, C. Guthmann, and S. de Cheveigné, Phys. Rev. A **42**, 7368 (1990).

[26] Simulations not reported in [7] show that, in channels with rigid walls and at sufficiently low Δ, the SB fingers themselves are unstable, being continually overgrown by tilted doublons arising from their sidebranches. In this case, the system never reaches a steady state. We do not observe this mode of instability experimentally.

[27] A. G. Borisov, O. P. Fedorov, and V. V. Maslov, J. Cryst. Growth **112**, 463 (1991).

[28] Y. Saito, G. Goldbeck-Wood, and H. Müller-Krumbhaar, Phys. Rev. Lett. **58**, 1541 (1987); Phys Rev. A **38**, 2148 (1988).

[29] Y. Saito and T. Sakiyama, J. Cryst. Growth **128**, 224 (1993). Note that the scale of $\ln\lambda$ in Fig. 1(b) of this reference is incorrect; it must be 1.0, 0.5, 0.0, -0.5, and -1.0 from the top to the bottom [Y. Saito (private communication)].

[30] H. Müller-Krumbhaar (private communication).

[31] There are systems, NH_4Cl, for instance [S.-K. Chan, H.-H. Reimer, and M. Kahlweit, J. Cryst. Growth **32**, 303 (1976)], in which an abrupt change in the growth direction of dendrites occurs as the undercooling increases, indicating that the orientation dependence of the surface tension and that of the kinetic coefficient are different. In such cases, the latter must be described by cubic spherical harmonics of order higher than 4. This is not the case for CBr_4.

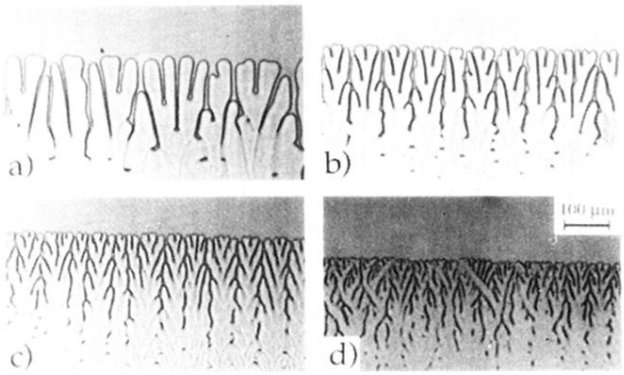

FIG. 10. Seaweed morphology in a crystal close to the {111} orientation. (a) $V=8.6\ \mu m\,s^{-1}$ ($\approx 4.5 V_{CS}$); (b) $V=29\ \mu m\,s^{-1}$ ($\approx 15 V_{CS}$); (c) $V=64\ \mu m\,s^{-1}$ ($\approx 34 V_{CS}$); (d) $V=100\ \mu m\,s^{-1}$ ($\approx 53 V_{CS}$).

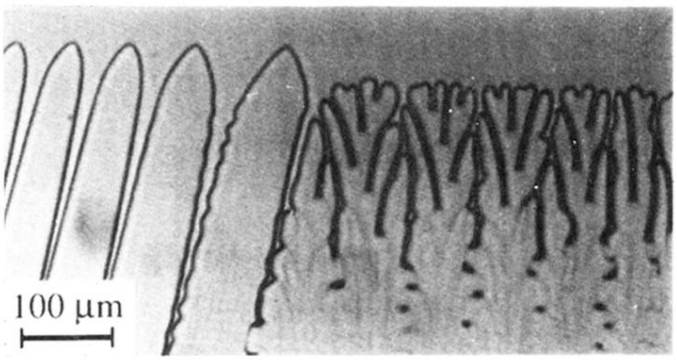

FIG. 11. Grain boundary between a tilted-dendritic grain and a seaweed grain. $V=29\ \mu\text{m s}^{-1}$ ($\approx 15 V_{CS}$).

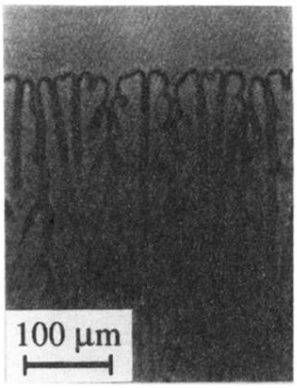

FIG. 15. A seaweed cell containing one doublon whose lifetime was about 30 s ($\approx 60\tau_d$). $V = 32\ \mu\text{m s}^{-1}$ ($\approx 17 V_{CS}$).

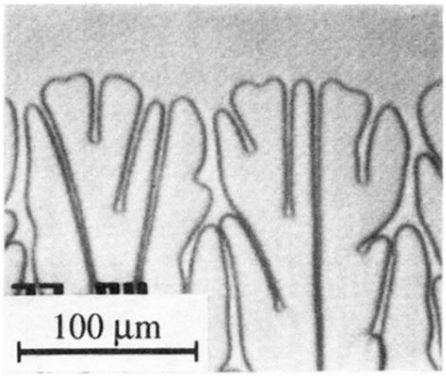

FIG. 17. Enlarged view of a seaweed pattern. $V=32\ \mu\mathrm{m\,s^{-1}}$ ($\approx 17 V_{CS}$). Note, from left to right, a doublon joining a wide groove, a newly created doublon, and a triplet structure.

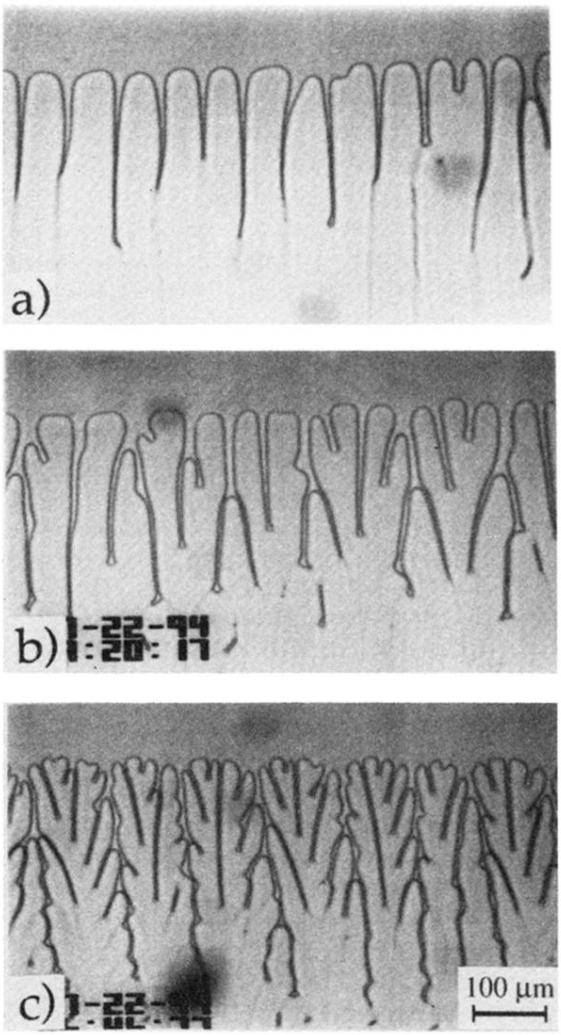

FIG. 18. The low-velocity transition in a nearly {111}-oriented grain. (a) $V=4\ \mu m\ s^{-1}$ ($\approx 2.1 V_{CS}$). (b) 8.5 $\mu m\, s^{-1}$ ($\approx 4.5 V_{CS}$); (c) 32 $\mu m\, s^{-1}$ ($\approx 17 V_{CS}$).

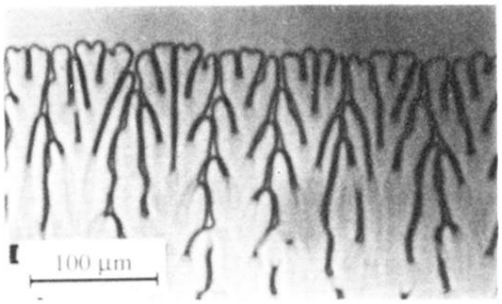

FIG. 2. Seaweed pattern in a nearly {111}-oriented crystal. The growth direction is upward, as for all the photographs in this article. The pulling velocity $V = 64\ \mu\text{m s}^{-1} (\approx 33.7 V_{\text{CS}})$.

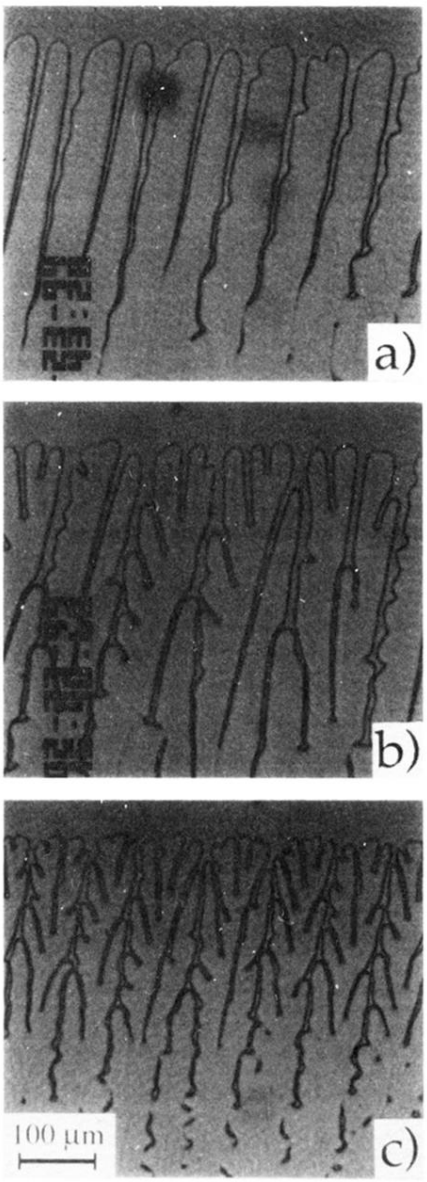

FIG. 21. Tilted-seaweed morphology in a crystal close to (but not exactly in) the (111) orientation. (a) $V=12.5$ $\mu m\,s^{-1}$ ($\approx 6.5 V_{CS}$); (b) $V=19.6$ $\mu m\,s^{-1}$ ($\approx 10.3 V_{CS}$); (c) $V=32$ $\mu m\,s^{-1}$ ($\approx 16.8 V_{CS}$).

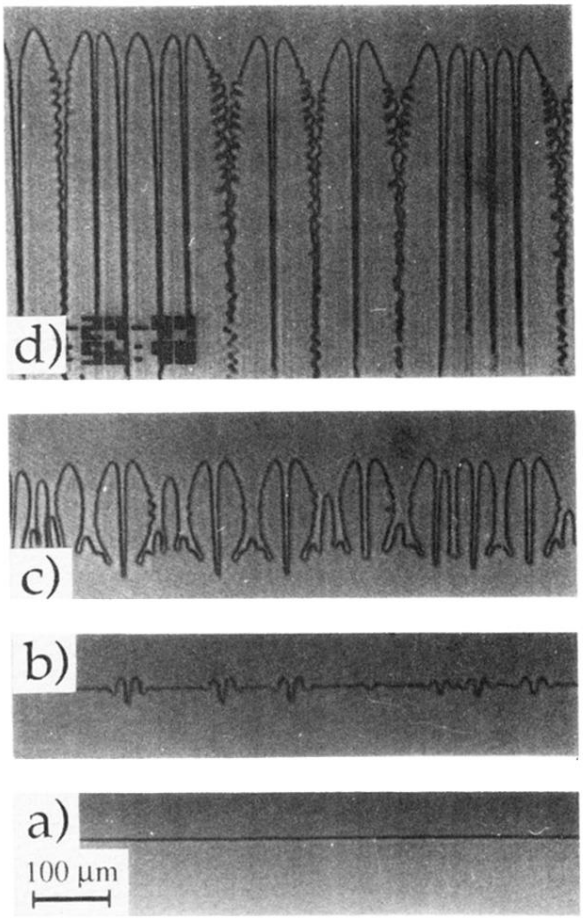

FIG. 22. Crystal close to the (001)[100] orientation. Initial transient of the first run at $V=103\ \mu m\,s^{-1}$ ($V\approx 54V_{CS}$; $l_d=4.9\ \mu m$; $\tau_d=0.05$ s). (a) $t=0$ s (onset of the pulling); (b) $t=6.4$ s; (c) $t=8.1$ s; (d) $t=42$ s. Note the dendritic doublons in the middle and the multiplet on the right. The tilt angle of the dendrites is about 2°, with a negligible dispersion.

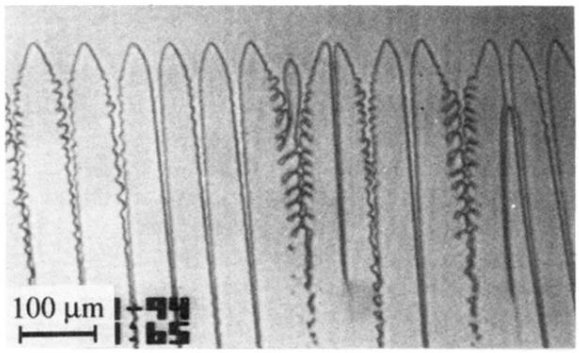

FIG. 23. Same grain as in Fig. 22. Second run at $V=103$ $\mu m\,s^{-1}$. The tilt angle of the dendrites is $5°\pm2°$. This figure corresponds to $t=90$ s in the ST diagram shown in Fig. 24. Note the source operating by a tail-instability mechanism next to the doublon.

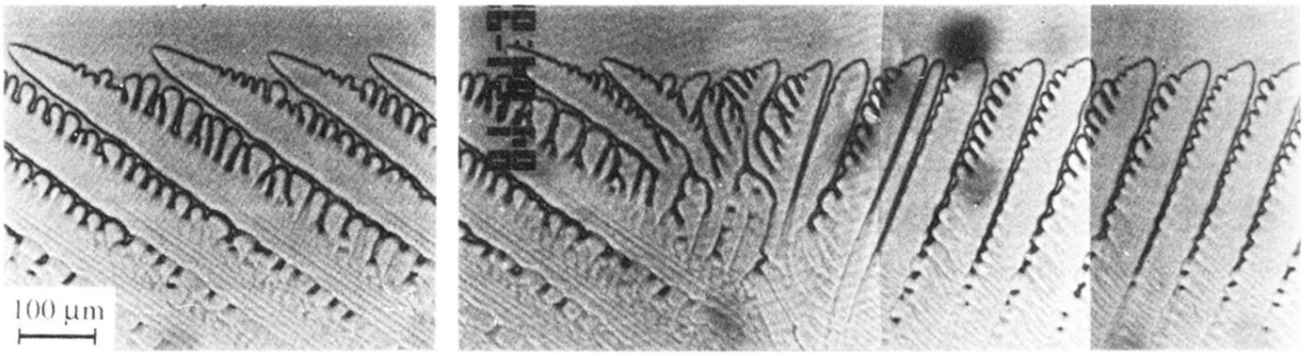

FIG. 25. Competition between two tilted dendritic states in a crystal close to the degenerate orientation (same crystal as in Fig. 4). $V=32\ \mu\text{m s}^{-1}$ ($\approx 17V_{CS}$). Note the dynamic wall between two domains occupied by the [100] ($\phi\approx 22°$ to the right) and the [010] dendritic states ($\phi\approx 54°$ to the left), respectively.

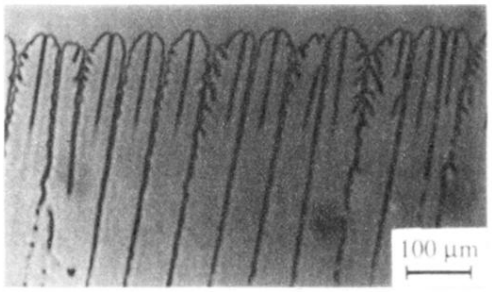

FIG. 3. Doublons in a nearly $\{001\}\langle 100\rangle$-oriented crystal. $V = 103\ \mu\text{m s}^{-1} \approx 27 V_{CS}$ ($C_\infty \approx 4\%$ in this experiment).

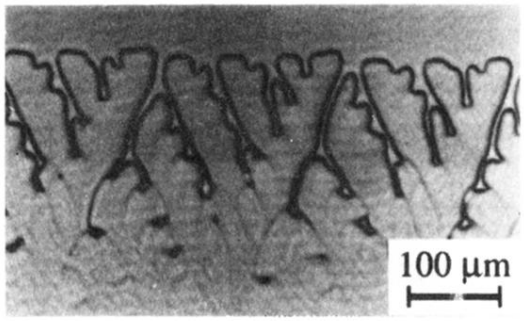

FIG. 4. Degenerate pattern in a nearly {001}⟨110⟩-oriented grain. $V=7\ \mu\text{m s}^{-1}$ ($\approx 3.7 V_{CS}$).

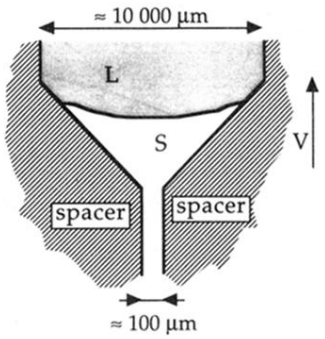

FIG. 6. Sketch of the method of obtaining single crystals (L, liquid; S, solid).

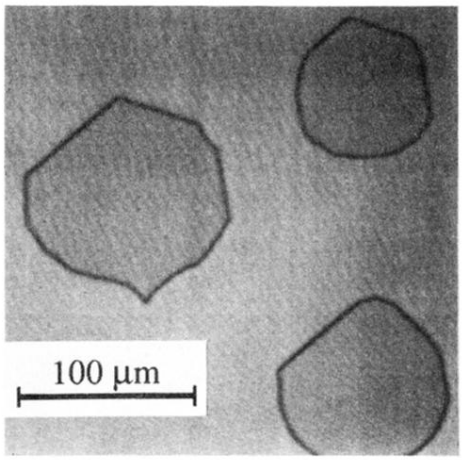

FIG. 7. Partly faceted residual-gas inclusions in a nearly {111}-oriented crystal. Note that the orientation of the facets is the same in all the inclusions.

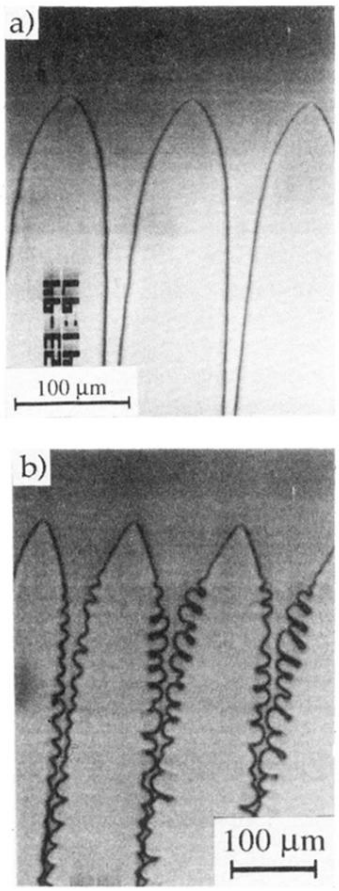

FIG. 8. Dendrite tips in a nearly {001}⟨100⟩-oriented crystal (see Table III). (a) $V=13\ \mu m\ s^{-1}$; (b) $V=35\ \mu m\ s^{-1}$.

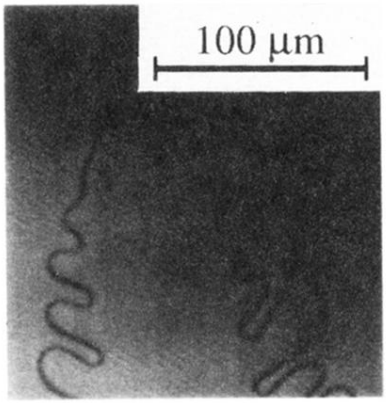

FIG. 9. Dendrite tip in a crystal relatively close to a {111} orientation (off-plane misorientation angle $\approx 7°$). $V = 14$ $\mu m\,s^{-1}$.